Adiabatic States Derived from a Spin-Coupled Diabatic Transformation: Semiclassical Trajectory Study of Photodissociation of HBr and the Construction of Potential Curves for LiBr$^+$

Rosendo Valero and Donald G. Truhlar*

Department of Chemistry and Supercomputing Institute, University of Minnesota, Minneapolis, Minnesota 55455-0431

Ahren W. Jasper*

Combustion Research Facility, Sandia National Laboratories, P. O. Box 969, Livermore, California 94551-0969

The development of spin-coupled diabatic representations for theoretical semiclassical treatments of photodissociation dynamics is an important practical goal, and some of the assumptions required to carry this out may be validated by applications to simple systems. With this objective, we report here a study of the photodissociation dynamics of the prototypical HBr system using semiclassical trajectory methods. The valence (spin-free) potential energy curves and the permanent and transition dipole moments were computed using high-level ab initio methods and were transformed to a spin-coupled diabatic representation. The spin−orbit coupling used in the transformation was taken as that of atomic bromine at all internuclear distances. Adiabatic potential energy curves, nonadiabatic couplings and transition dipole moments were then obtained from the diabatic ones and were used in all the dynamics calculations. Nonadiabatic photodissociation probabilities were computed using three semiclassical trajectory methods, namely, coherent switching with decay of mixing (CSDM), fewest switches with time uncertainty (FSTU), and its recently developed variant with stochastic decoherence (FTSU/SD), each combined with semiclassical sampling of the initial vibrational state. The calculated branching fraction to the higher fine-structure level of the bromine atom is in good agreement with experiment and with more complete theoretical treatments. The present study, by comparing our new calculations to wave packet calculations with distance-dependent ab initio spin−orbit coupling, validates the semiclassical trajectory methods, the semiclassical initial state sample scheme, and the use of a distance-independent spin−orbit coupling for future applications to polyatomic photodissociation. Finally, using LiBr$^+$ as a model system, it is shown that accurate spin-coupled potential curves can also be constructed for odd-electron systems using the same strategy as for HBr.

1. Introduction

Hydrogen halides (HX, with X = F, Cl, Br, I) absorb radiation in the ultraviolet region of the spectrum. Excitation to their first absorption continuum (A-band) causes prompt dissociation into two different channels:

$$HX(X\ ^1\Sigma^+) \xrightarrow{h\nu} H(^2S) + X(^2P_{3/2})$$

$$HX(X\ ^1\Sigma^+) \xrightarrow{h\nu} H(^2S) + X(^2P_{1/2}) \quad (1)$$
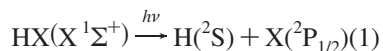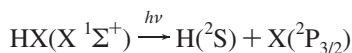
with the halogen atom in its ground ($J = 3/2$) or excited ($J = 1/2$) fine-structure level. In the absence of spin−orbit coupling (SOC), four electronic states ($X^1\Sigma^+$, $^1\Pi$, $^3\Sigma^+$, and $^3\Pi$), of which only the ground state ($^1\Sigma^+$) is bound, correlate with ground-state atomic fragments. The excited electronic states in the A-band differ from the ground-state by either a $\pi \rightarrow \sigma^*$ ($^1\Pi$ and $^3\Pi$) or a $\sigma \rightarrow \sigma^*$ ($^3\Sigma^+$) electronic excitation, which explains

their repulsive character and the broad and featureless absorption band observed experimentally. The spin−orbit interaction mixes and splits the singlet and triplet electronic states and modulates the branching to the product states by changing both the partial absorption cross sections in the Franck−Condon (FC) region and the subsequent multistate dissociation dynamics. The systematic increase in the magnitude of SOC in the series X = F, Cl, Br, I offers a unique opportunity to study the factors controlling the reaction dynamics in these systems, in particular, the branching ratio between the two fine-structure levels of the halogen atom. This feature, along with the simplicity of the hydrogen halides, explains their role as prototypical systems in this area.

In recent years, many experimental and theoretical studies have been devoted to the photodissociation of the different hydrogen halides (HF,[1–4] HCl,[5–15] HBr,[16–28] and HI[29–40]) and have provided, among other properties, absorption cross sections and branching fractions to the excited fine-structure level of the halogen. These studies were preceded by many classical experimental studies.[41–45] The branching fraction is defined, in the specific case of HBr, as

* Corresponding authors. E-mail: truhlar@umn.edu (D.G.T.); jasper@ sandia.gov (A.W.J.).

$$\Gamma = \frac{\sigma[\text{Br*}]}{\sigma[\text{Br}] + \sigma[\text{Br*}]} \qquad (2)$$

where $\sigma[\text{Br}]$ and $\sigma[\text{Br*}]$ denote, respectively, the partial photodissociation cross sections at a particular photon wavelength to the ground and the excited fine-structure levels of bromine. An accurate prediction of the branching fraction is a stringent test of the quality of the underlying potential and transition dipole moment curves[46] as well as of the dynamic methods employed to study the photofragmentation dynamics.

The experimental absorption spectrum of hydrogen bromide has been measured between 230 and 170 nm (corresponding to photon energies between about 43 500 and 59 000 cm^{-1}).[43] The spectrum has a bell shape with a maximum at 176 nm (56 800 cm^{-1}). Experimental determinations of the branching fraction were limited until recently to only a few different wavelengths. Thus, an early value of 0.15 was reported following photolysis of HBr at 193 nm[16] and a comparable value (0.14) was obtained more recently using the technique of velocity-aligned Doppler spectroscopy of the H atom at the same wavelength.[17,18] In another study using a combination of ion imaging and Doppler spectroscopy, a value of 0.14 was reported at 243 nm.[20] A time-of-flight mass spectrometric study was conducted at three wavelengths (193, 205, and 243 nm), obtaining branching fractions of 0.18, 0.18, and 0.20, respectively.[23] The most extensive study to date involved the determination of the branching fractions at 15 different wavelengths in the range 201−253 nm, using the technique of H Rydberg atom photofragment translational spectroscopy.[23] The fraction of the total flux going to the excited bromine channel varies from about 0.15 at the shortest and longest wavelengths to about 0.22−0.23 at the maximum (235 nm, 42 500 cm^{-1}). Interestingly, the maximum branching fraction is the smallest among the hydrogen halides. This observation has been discussed in terms of the interplay of the two factors mentioned above, namely, absorption intensity in the FC region and nonadiabatic redistribution of the dissociation flux.[24] It has been suggested that both effects are important for HBr, whereas one or the other mechanism dominates for the other HX molecules.

Previous theoretical studies of the photodissociation dynamics of HBr are relatively scarce.[21,22,27] In one study,[21] three different methods (time-independent and time-dependent quantum dynamic methods, and a semiclassical method) were used to obtain product branching ratios at two different wavelengths (193 and 243 nm). The results obtained with the three methods agree reasonably well with each other and with the experimental branching ratios at those wavelengths. In an extension[22] of this work, the dependence of the photodissociation dynamics on the initial vibrational level on the ground electronic state was considered. The branching ratios for vibrationally excited HBr showed oscillations when plotted versus the photon energy, reflecting the nodes in the vibrational wave functions. The same behavior has been observed for HF,[3] HCl,[5,8,13] and HI.[30,31,34,36,37] Recently, an extensive investigation of the photodissociation dynamics of HBr using time-dependent wave packet dynamics on a set of high-level ab initio potential energy and transition dipole moment curves has been reported.[27] The authors obtained good agreement with experiment for the partial and total cross sections, branching fractions, and anisotropy parameters describing the angular momentum vector correlations of the photofragments.

In this work we report a study of the total and partial photodissociation cross sections of HBr and of the branching fraction to the excited-state bromine channel. The main goal of the present study is to test the performance of a combined electronic structure and dynamic scheme that can readily be applied to larger molecules. In particular, we test the assumption of using a constant SOC and a spin-coupled diabatic representation in the construction of the potential and transition dipole moment curves combined with semiclassical trajectory methods for the dynamics and semiclassical sampling of vibrational motion for the initial conditions. When we specify a representation as diabatic we mean that the coupling due to the nuclear momentum and kinetic energy are assumed negligible in that representation (this is sometimes called quasidiabatic).

In section 2.1 the ab initio methods used to calculate the spin-free potential energies and permanent and transition dipole moments are detailed. The methods are essentially those employed in ref 27, with the important difference that here the (experimental) SOC constant of atomic bromine is used at all internuclear distances. Section 2.2 contains a description of the analytical functions used to fit the diabatic potential matrix and the adiabatic potential energy, nonadiabatic coupling, and transition dipole moment curves. The nonadiabatic coupling in the adiabatic representation derives entirely from the diabatic-to-adiabatic transformation. The classical FC sampling employed to simulate the photon absorption is explained in section 2.3. The non-Born−Oppenheimer (non-BO) semiclassical trajectory methods used to compute the photodissociation dynamics are the subject of section 2.4. In section 3, the calculated adiabatic and nonadiabatic partial and total cross sections and the branching fractions to the excited fine-structure level of bromine are compared with experiment and with previous theoretical work. The extension of the constant-SOC approximation to an odd-electron system is presented in section 4 with an application to the LiBr$^+$ diatomic molecule. Section 5 contains the conclusions.

2. Methods

2.1. Electronic Structure. Four spin-free electronic states (X$^1\Sigma^+$, $^1\Pi$, $^3\Sigma^+$, and $^3\Pi$) correlate with the open-shell ground-state spin-free atoms, H(^{2}S) + Br(^{2}P). These electronic states represent a total of 12 substates (one for X$^1\Sigma^+$, two for $^1\Pi$, three for $^3\Sigma^+$, and six for $^3\Pi$), characterized by well-defined values of Λ and Σ, the projections of the electronic and spin angular momenta, respectively, on the internuclear axis. Eigenstates of the sum of the electronic Hamiltonian and the spin−orbit Hamiltonian may be constructed as linear combinations of the spin-free substates. In this way, eight electronic potential energy curves are generated, characterized by the absolute value of the projection of the total electronic angular momentum Ω on the internuclear axis. The states with $\Omega = 0$ are nondegenerate, and the states with $\Omega = 1$ and 2 are doubly degenerate. In a mixed Hund's case (a)/(c) notation, the ground state is denoted as X$^1\Sigma_{0^+}$, and the excited states are denoted as $^3\Pi_2$, $^3\Pi_1$, $^3\Pi_{0^+}$, $^3\Pi_{0^-}$, $^1\Pi_1$, $^3\Sigma_{0^-}$, and $^3\Sigma_1$. Henceforth the spin-coupled adiabatic substates will be numbered as follows: 1, X$^3\Sigma_{0^+}$; 2 and 3, $^3\Pi_2$; 4 and 5, $^3\Pi_1$; 6, $^3\Pi_{0^-}$; 7, $^3\Pi_{0^+}$; 8 and 9, $^1\Pi_1$; 10, $^3\Sigma_{0^-}$; 11 and 12, $^3\Sigma_1$. In this work we neglect the rotational Hamiltonian, since rotation has been found to have an almost negligible effect on the photodissociation dynamics for all the hydrogen halides.[2,5,7,13,22,34,35,39] The excited electronic states of HBr that can be accessed from the ground state by absorption of a photon are, in the electric dipole approximation and in the absence of rotation, those that fulfill the $\Delta\Omega = 0$, ± 1 and the $0^\pm \leftrightarrow 0^\pm$ selection rules, that is, $^1\Pi_1$, $^3\Pi_1$, $^3\Pi_{0^+}$, and $^3\Sigma_1$. Adiabatically, the first two states correlate with the ground fine-structure level of bromine, and the last two correlate with the excited fine-structure level. The electronic states that contribute significantly to the absorption spectrum of HBr in the A-band are the same as those predicted by Mulliken for

HI,[47,48] namely, $^1\Pi_1$, $^3\Pi_1$, and $^3\Pi_{0^+}$, whereas the $^3\Sigma_1$ state of HBr is too high in energy to contribute significantly to the total absorption intensity in this spectral region.[27] Without rotational coupling, only states with the same value of Ω can interact. Along with the selection rule for absorption, this determines that, to a good approximation, the electronic states relevant to the photodissociation of HBr fall into the two noninteracting subsets of states $\{X^1\Sigma_{0^+}, {}^3\Pi_{0^+}\}$ and $\{^1\Pi_1, {}^3\Pi_1, {}^3\Sigma_1\}$.

The calculation of the valence (spin-free) adiabatic potential energy and permanent and transition dipole moment curves for the $X^1\Sigma^+$, $^1\Pi$, $^3\Sigma^+$, and $^3\Pi$ electronic states was carried out using the MOLPRO electronic structure program.[49] The aug-cc-pV5Z[50] basis set was used for hydrogen, and the aug-cc-pV5Z-PP[51,52] basis set, which includes a small-core relativistic pseudopotential for the core electrons, was used for bromine. The state-averaged complete-active-space self-consistent field (SA-CASSCF) method[53,54] was employed to generate a set of configuration-interaction (CI) coefficients and molecular orbitals (MOs) for the spin-free electronic states. The four electronic states ($X^1\Sigma^+$, $^1\Pi$, $^3\Sigma^+$, and $^3\Pi$) were included in the state averaging with equal weights. The active space contains six electrons in four molecular orbitals (σ, σ^*, and two nonbonding Π MOs). Subsequently, the internally contracted multireference CI (IC-MRCI) method[55–57] was used to include all the single and double excitations from the SA-CASSCF(6,4) reference space. The multireference version[58,59] of Davidson's correction for quadruple excitations[60] was computed and added to the IC-MRCI energies; as usual the resulting energies are called IC-MRCI+Q.

In general, to study electronically nonadiabatic chemical reactions, it is convenient to work in a diabatic representation because the diabatic energies and couplings are smooth functions of the nuclear coordinates and the couplings are scalar quantities.[60–75] For systems in which nonadiabatic interactions are partially or totally caused by SOC, we have recently developed a procedure for constructing a diabatic representation for single-bond and multibond dissociation reactions (i.e., for dissociation of bonds between one or several atoms carrying SOC and the rest of the molecule).[76] The procedure used for single-bond reactions is briefly summarized next.

The procedure for including SOC allows one to construct adiabatic and diabatic representations of both the valence (spin-free) electronic Hamiltonian and the total (valence + spin−orbit) electronic Hamiltonian (see Table 1 of ref 76). The valence adiabatic representation is the representation that diagonalizes the electronic Hamiltonian, and the valence diabatic (strictly, quasidiabatic[77]) representation is the one that minimizes the nonadiabatic couplings between the spin-free electronic states. Likewise, in the fully adiabatic representation the matrix of the total (spin-inclusive) electronic Hamiltonian is diagonal, and the fully diabatic representation minimizes the nonadiabatic couplings between the spin-coupled states. We call these representations V-adiabatic, V-diabatic, F-adiabatic, and F-diabatic, respectively. The full classification is especially useful for low-symmetry polyatomics.

For HBr, the spin-free electronic states studied in this work differ from one another by their spin and/or spatial symmetry and are uncoupled in the absence of SOC. The V-adiabatic and the V-diabatic representation are therefore equivalent. The valence adiabatic or diabatic matrix for HBr is a 12×12 diagonal matrix with the IC-MRCI+Q energies as its diagonal elements

$$H_{\alpha\alpha'}^{\text{Val}}(r) = E_\alpha(r)\delta_{\alpha\alpha'}, \quad 1 \le \alpha \le 12 \quad (3)$$

where "α" labels the V-diabatic substates and r is the H−Br internuclear distance. The zero of energy is chosen as the energy

of the 12-fold degenerate V-diabatic substates in the dissociation limit, $H(^2S) + Br(^2P)$.

Diagonalization of the asymptotic spin−orbit matrix in the V-diabatic representation provides the transformation matrix to the F-diabatic representation. This matrix is here denoted as $\mathbf{C}^{(12)}$:

$$\mathbf{H}^{\text{SO,F-d}}(\infty) = \mathbf{C}^{(12)\dagger}\mathbf{H}^{\text{SO,Val}}(\infty)\mathbf{C}^{(12)} \quad (4)$$

where $\mathbf{H}^{\text{SO,F-d}}(\infty)$ is a diagonal matrix with eight elements equal to the energy of the $H(^2S) + Br(^2P_{3/2})$ fine-structure level, $-\Delta E_{\text{SO,Br}}/3$, and four elements equal to the energy of the $H(^2S) + Br(^2P_{1/2})$ level, $2\Delta E_{\text{SO,Br}}/3$, with $\Delta E_{\text{SO,Br}}$ being the experimental fine-structure splitting of the bromine atom (3685 cm^{-1} or 0.46 eV).[78] The F-diabatic potential energy matrix is finally obtained as

$$\mathbf{H}^{\text{F-d}}(r) = \mathbf{C}^{(12)\dagger}\mathbf{H}^{\text{Val}}(r)\mathbf{C}^{(12)} + \mathbf{H}^{\text{SO,F-d}}(\infty) \quad (5)$$

Diagonalization of the F-diabatic potential matrix yields the F-adiabatic matrix, $\mathbf{H}^{\text{F-a}}(r)$. A set of F-adiabatic potential energies $E_j^{\text{F-a}}(r)$ could be obtained, in principle, as the eigenvalues of the fitted analytical F-diabatic potential energy matrix "on-the-fly" at each molecular configuration along a semiclassical trajectory simulation. However, for the high-symmetry case of a diatomic molecule such as HBr, the energies of some of the roots obtained by diagonalization of the F-diabatic matrix cross along the dissociation coordinate. This causes some difficulties because, in trajectory simulations, the F-adiabatic energies and the expansion coefficients of each F-adiabatic state in the F-diabatic basis set must vary continuously along the dissociation coordinate. Otherwise, discontinuities in the energy gradients and in the nonadiabatic couplings would arise. To avoid this difficulty, the eigenstates of the F-diabatic potential matrix have been reordered by taking the overlap of a vector of their expansion coefficients at consecutive points as the ordering criterion. The eigenvalues were reordered simultaneously with the eigenstates. The matrix containing the reordered F-adiabatic potential curves on the diagonal will be denoted as $\mathbf{E}^{\text{F-a}}(r)$. A plot of the diagonal elements of $\mathbf{E}^{\text{F-a}}(r)$ is shown in Figure 1. Then, nonadiabatic couplings are calculated by the multistate generalization of the two-state expression of a previous study[79]

$$d_{ij}(r) = \frac{1}{E_{jj}^{\text{F-a}}(r) - E_{ii}^{\text{F-a}}(r)} \sum_{k,l=1}^{12} c_{ki}(r)\, c_{lj}(r) \nabla H_{k,l}^{\text{F-d}}(r), \quad 1 \le$$

$$i, j \le 12, \, i \ne j \quad (6)$$

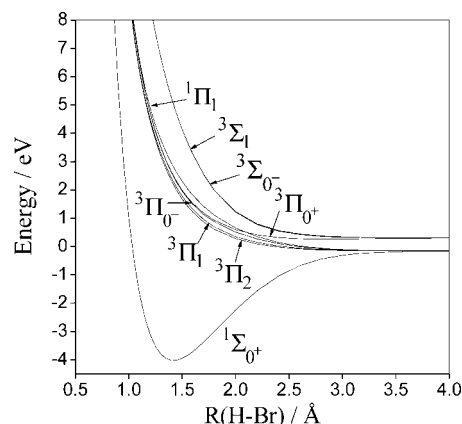where $\{c_{ki}(r), 1 \le k \le 12\}$ and $\{c_{lj}(r), 1 \le l \le 12\}$ are the

Figure 1. F-adiabatic potential energy curves (diagonal elements of the $\mathbf{E}^{\text{F-a}}(r)$ matrix) for the HBr molecule obtained in fit A using the experimental SOC constant of bromine.

Photodissociation of HBr

J. Phys. Chem. A, Vol. 112, No. 25, 2008 **5759**

expansion coefficients of the i and j F-adiabatic states, after the reordering explained above, in the F-diabatic basis set.

In this work all the calculations of absorption spectra and photodissociation cross sections are carried out in the F-adiabatic representation.

2.2. Analytic Potential, Nonadiabatic Coupling, and Transition Dipole Moment Functions. In this section we explain in detail the procedure used to obtain the F-adiabatic potential energies, nonadiabatic couplings, and transition dipole moments and their fitting to analytical functions to be used in subsequent semiclassical dynamics simulations.

First, the V-diabatic IC-MRCI+Q potential energies and IC-MRCI permanent and transition dipole moments were computed at 50 different H−Br distances in the range 0.85−9.0 Å. The IC-MRCI+Q potential energies, the experimental bromine SOC constant, and the $\mathbf{C}^{(12)}$ transformation matrix were used as in eqs 3–5 to construct the F-diabatic potential matrix. The 12 F-diabatic potential energy curves (of which only eight are unique) were fitted to expressions of the form[80]

$$H_{i,i}^{F\text{-}d}(r) = F_i^{short}(r) + (F_i^{long}(r) - F_i^{short}(r))T_i(r) +$$
$$f\Delta E_{SO,Br}, \quad 1 \le i \le 12 \quad (7)$$

where the short-range function is a 10-term sum of Gaussians

$$F_i^{short}(r) = \sum_{K=1}^{10} c_{i,K}\exp(-\alpha_{i,K}(r - r_{i,K}^0)^2), \quad 1 \le i \le 12 \quad (8)$$

the long-range function is a sum of inverse powers of the internuclear distance

$$F_i^{long}(r) = \frac{c_{i,11}}{r^6} + \frac{c_{i,12}}{r^8} + \frac{c_{i,13}}{r^{10}}, \quad 1 \le i \le 12 \quad (9)$$

and $T_i(r)$ is a switching function that connects smoothly the short- and long-range terms

$$T_i(r) = 0.5[1 + \tanh(a_i(r - b_i))], \quad 1 \le i \le 12 \quad (10)$$

In eq 7, f is equal to $-1/3$ for the F-diabatic states that correlate with H(^{2}S) + Br(^{2}P$_{3/2}$) (two states with $\Omega = 2$, two states with $\Omega = 1$, one state with $\Omega = 0^+$ symmetry, and one state with $\Omega = 0^-$ symmetry) and $2/3$ for the states that correlate with H(^{2}S) + Br(^{2}P$_{1/2}$) (one state with $\Omega = 1$, one state with $\Omega = 0^+$ symmetry, and one state with $\Omega = 0^-$ symmetry). The F-diabatic states can be ordered as the columns of the transformation matrix $\mathbf{C}^{(12)}$ (see Table 3 in ref 76). Following this ordering, the F-diabatic energies are labeled as follows: $H_{1,1}^{F\text{-}d}(r)$ ($\Omega = 0^+$, $J = 3/2$), $H_{2,2}^{F\text{-}d}(r)$ ($\Omega = 2$, $J = 3/2$), $H_{3,3}^{F\text{-}d}(r)$ ($\Omega = 0^+$, $J = 1/2$), $H_{4,4}^{F\text{-}d}(r)$ ($\Omega = 1$, $J = 3/2$), $H_{5,5}^{F\text{-}d}(r)$ ($\Omega = 1$, $J = 1/2$), $H_{6,6}^{F\text{-}d}(r)$ ($\Omega = 1$, $J = 3/2$), $H_{10,10}^{F\text{-}d}(r)$ ($\Omega = 0^-$, $J = 1/2$), and $H_{12,12}^{F\text{-}d}(r)$ ($\Omega = 0^-$, $J = 3/2$). The remaining states are degenerate with one of the mentioned states; thus, the following equalities are fulfilled:

$$H_{7,7}^{F\text{-}d}(r) = H_{4,4}^{F\text{-}d}(r)$$
$$H_{8,8}^{F\text{-}d}(r)$$
$$= H_{5,5}^{F\text{-}d}(r)$$
$$H_{9,9}^{F\text{-}d}(r)$$
$$= H_{6,6}^{F\text{-}d}(r)$$
$$H_{11,11}^{F\text{-}d}(r)$$
$$= H_{2,2}^{F\text{-}d}(r) \quad (11)$$

The root-mean-square (rms) errors of the fits to the F-diabatic

states are generally less than 1 meV, with a maximum of about 5 meV. The parameters of the fits are given in Table S1 of Supporting Information.

The five unique nonzero F-diabatic couplings were fitted to the same type of expression as the F-diabatic energies, but the form of the short-range term was chosen as a 10-term even-tempered sum of Gaussians

$$F_{ij}^{short}(r) = \sum_{K=0}^{9} c_{ij,K}\exp(-\alpha_{ij}\beta_{ij}^K(r - r_{0,ij})^2) \quad (12)$$

where the ij indexes refer to the following elements of the F-diabatic matrix: $H_{1,3}^{F\text{-}d}(r)$ $H_{4,5}^{F\text{-}d}(r)$, $H_{4,6}^{F\text{-}d}(r)$, $H_{5,6}^{F\text{-}d}(r)$, and $H_{10,12}^{F\text{-}d}(r)$. The following equalities

$$H_{7,8}^{F\text{-}d}(r) = -H_{4,5}^{F\text{-}d}(r)$$
$$H_{7,9}^{F\text{-}d}(r) = -H_{4,6}^{F\text{-}d}(r)$$
$$H_{8,9}^{F\text{-}d}(r) = -H_{5,6}^{F\text{-}d}(r) \quad (13)$$

and the fact that the F-diabatic matrix is real symmetric permit obtaining all the nonzero diabatic couplings. In this case, none of the rms errors of the fits exceeds 1 meV. The parameters of the fits are given in Table S2 of Supporting Information.

The F-adiabatic potential energy curves have been also fitted to the expression in eq 7, obtaining rms errors of 1−2 meV. The parameters of the fits are given in Table S3 of Supporting Information. The accuracy of the fitted ground-state (X$^1\Sigma_{0^+}$) F-adiabatic potential energy curve can be assessed by comparing its spectroscopic parameters with experiment. The theoretical equilibrium distance (r_e) and the vibrational harmonic frequency (ω_e) are equal to 1.4190 Å and 2648.3 cm^{-1}, respectively, compared with the experimental values 1.4144 Å and 2649.0 cm^{-1}.[81] The equilibrium dissociation energy D_e obtained from the fits is equal to 3.88 eV, and the zero-point dissociation energy D_0 calculated assuming a harmonic vibration is equal to 3.72 eV, in good agreement with the experimental values, 3.92 eV[81] and 3.746 ± 0.005 eV,[24] respectively.

The nonadiabatic couplings between the F-adiabatic states can be obtained numerically once the F-diabatic matrix and the $\mathbf{E}^{F\text{-}a}$ matrix with the reordered F-adiabatic energies are known. In eq 6 note that

$$\nabla H_{k,l}^{F\text{-}d}(r) = \nabla H_{l,k}^{F\text{-}d}(r) \quad (14)$$

The four unique scalar nonadiabatic coupling curves have been fitted as follows. First, the factor in front of the sum in eq 6, containing the F-adiabatic energy differences in the denominator, was left out, and the remainder was fitted to five-term sums of even-tempered Gaussian functions

$$d_{ij}(r) = \sum_{K=1}^{5} c_{ij,K}\exp(-\alpha_{ij}\beta_{ij}^K(r - r_{ij,K})^2) \quad (15)$$

where ij denotes the following four pairs of states: X$^1\Sigma_{0^+}$−$^3\Pi_{0^+}$, $^1\Pi_1$−$^3\Pi_1$, $^3\Pi_1$−$^3\Sigma_1$, and $^1\Pi_1$−$^3\Sigma_1$. The fitted functions were then divided by the F-adiabatic energy differences, and the resulting nonadiabatic couplings were fitted to the same functional forms of eq 15. This two-step procedure was necessary in order to avoid spurious nonzero couplings at long internuclear distances. The rms errors obtained in the fits are of at most 10^{-2} Å^{-1}. The fitted nonadiabatic coupling curves are shown in Figure 2. The parameters of the fits are given in Table S4 of Supporting Information.

Finally, to determine the absorption cross sections, it is necessary to obtain the transition dipole moment functions. The
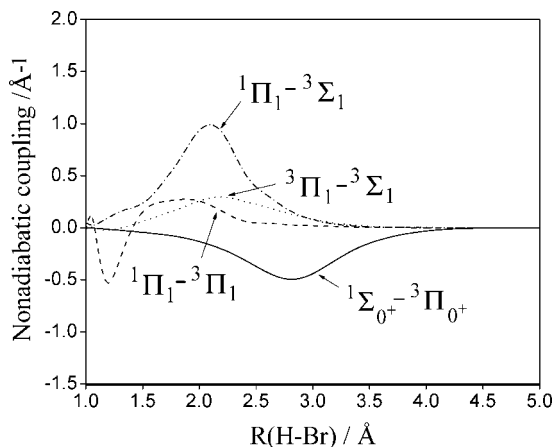
Figure 2. Nonadiabatic coupling curves for the HBr molecule obtained in fit A.

Figure 3. Transition dipole moment curves in atomic units (1 au of dipole moment = $1 ea_0$) for the HBr molecule obtained in fit A.

matrix containing the V-diabatic permanent dipole moments for the $X^1\Sigma^+$, $^1\Pi$, $^3\Sigma^+$, and $^3\Pi$ electronic states and the V-diabatic $^1\Sigma^+ \leftrightarrow {}^1\Pi$ and $^3\Sigma^+ \leftrightarrow {}^3\Pi$ transition dipole moments was computed at the IC-MRCI level and was transformed to the F-adiabatic representation. The distance-dependent transformation matrix $\mathbf{D}^{(12)}(r)$ was obtained by diagonalizing the sum of the electronic Hamiltonian matrix at the given H−Br distance and the spin−orbit Hamiltonian at the dissociation limit:

$$\mathbf{H}^{\text{F-a}}(r) = (\mathbf{D}^{(12)}(r))^{\dagger}(\mathbf{H}^{\text{Val}}(r) + \mathbf{H}^{\text{SO,Val}}(\infty))\mathbf{D}^{(12)}(r) \quad (16)$$

The columns of the transformation matrix are the eigenvectors of the F-diabatic potential matrix. For a diatomic molecule, the dipole moment vectors for a particular electronic state have nonzero Cartesian components either only parallel (μ_z) or only perpendicular (μ_x and μ_y) to the molecular axis, and the two perpendicular components are equal. The matrix containing the xy Cartesian components and that containing the z Cartesian components of $\boldsymbol{\mu}^{\text{Val}}(r)$ were transformed separately:

$$\mu_{xy}^{\text{F-a}}(r) = \mathbf{D}^{(12)}(r)^{\dagger} \, \mu_{xy}^{\text{Val}}(r) \, \mathbf{D}^{(12)}(r) \quad (17)$$

$$\mu_{z}^{\text{F-a}}(r) = \mathbf{D}^{(12)}(r)^{\dagger} \, \mu_{z}^{\text{Val}}(r) \, \mathbf{D}^{(12)}(r) \quad (18)$$

Thus, the F-adiabatic transition dipole moment vector for the only nonzero parallel transition from the ground state, namely, the one to the $^3\Pi_{0^+}$ state (which fulfills the $\Delta\Omega = 0$ and $0^+ \leftrightarrow 0^+$ selection rules, see above), is defined as

$$\boldsymbol{\mu}_{3\Pi_{0^+}}^{\text{F-a}}(r) = (0, 0, \mu_{ij,z}^{\text{F-a}}(r)), \quad i = 1, j = 7 \quad (19)$$

The magnitude of the F-adiabatic transition dipole moment vectors for the $^3\Pi_1$ perpendicular ($|\Delta\Omega| = 1$) transition is defined as

$$\mu_{3\Pi_1}^{\text{F-a}}(r) = \sqrt{\frac{(\mu_{14,xy}^{\text{F-a}}(r))^2 + (\mu_{15,xy}^{\text{F-a}}(r))^2}{2}} \quad (20)$$

with analogous definitions for $^1\Pi_1$ ($i = 1, j = 8, 9$) and $^3\Sigma_1$ ($i = 1, j = 11, 12$). The magnitudes of the four unique F-adiabatic transition dipole moments from the ground state to the $^3\Pi_{0^+}$, $^3\Pi_1$, $^1\Pi_1$, and $^3\Sigma_1$ excited states, which can be symbolized as $I = 1, 2, 3$, and 4, were fitted to five-term sums of even-tempered Gaussian functions

$$\mu_I^{\text{F-a}}(r) = \sum_{K=1}^{5} c_{I,K} \exp(-\alpha_I \beta_I^K (\xi - \xi_{I,K})^2), \quad 1 \leq I \leq 4 \, (21)$$

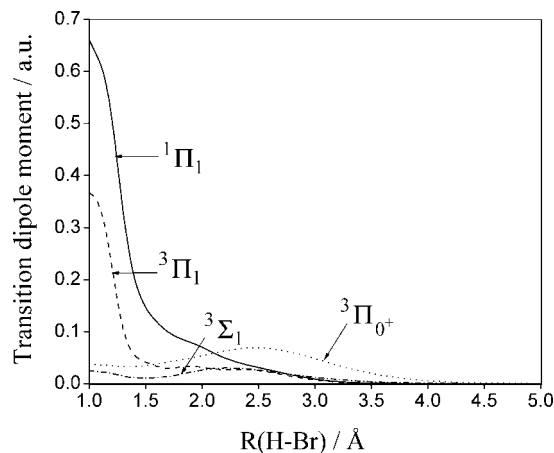where the variable ξ is defined as

$$\xi = \frac{r - 0.85 \, \text{Å}}{8.15 \, \text{Å}} \quad (22)$$

so that $\xi \in \{0, 1\}$ because ab initio transition dipole moments were computed at H−Br distances in the range 0.85−9.0 Å. The rms errors of these fits are all below 2×10^{-3} au, where 1 atomic unit (au) of dipole moment equals ea_0, where a_0 is a Bohr radius. The fitted F-adiabatic transition dipole moments are plotted in Figure 3. The parameters of the fits are given in Table S5 of Supporting Information. The curves compare very well to those reported in ref 27, except for the transition dipole moment to the $^3\Pi_{0^+}$ electronic state, which presents a substantially larger value in the FC region in the present work. This feature has an effect on the branching fraction to the excited fine-structure level of bromine which is large enough to improve the agreement with experiment significantly, as will be shown below.

The set of these fitted adiabatic energies, diabatic energies and couplings, nonadiabatic couplings, and transition dipole moments will be called fit A. All nonlinear-least-squares fits were carried out with a nonlinear Marquardt−Levenberg[82] least-squares algorithm. All linear and nonlinear fits were performed with the GNUPLOT program.[83]

2.3. Determination of Adiabatic Absorption Cross Sections. The broad absorption spectrum of HBr implies that the lifetime of the photoexcited HBr molecules is very short. Hence, it is reasonable to assume that all the excited molecules dissociate before they can return to the ground state by radiation, and that the total photoabsorption and photodissociation cross sections are identical. In the present study HBr is assumed to be initially in its nonrotating $v'' = 0$ vibrational level of the ground electronic state. In the absence of rotation, the expression for the quantum-mechanical partial absorption cross section from $v'' = 0$ on the ground electronic state (here denoted state number 1) to the continuum level ε of the nth F-adiabatic electronic state, where n represents any of the seven excited states $^3\Pi_2$, $^3\Pi_1$, $^3\Pi_{0^+}$, $^3\Pi_{0^-}$, $^1\Pi_1$, $^3\Sigma_{0^-}$, and $^3\Sigma_1$, is[84]

$$\sigma_{n\varepsilon,10}(\hbar\omega) = \frac{4\pi^2}{3\hbar c} \Delta E_{n\varepsilon,10} |\langle n\varepsilon|\mu_{n1}|10\rangle|^2 \delta(\hbar\omega - \Delta E_{n\varepsilon,10})$$

$$(23)$$

where $\hbar$ is Dirac's constant, c is the speed of light, ω is the photon frequency

$$\Delta E_{n\varepsilon,10} = E_{n\varepsilon} - (E_{1,1}^{\text{F-a}} + E_{\text{vib}}(v''=0)) \quad (24)$$

is the excitation energy, with $E_{\text{vib}}(v''=0)$ the vibrational zero-

Photodissociation of HBr

J. Phys. Chem. A, Vol. 112, No. 25, 2008 **5761**

point energy, $E_{n\varepsilon}$ is the total energy in the upper electronic state

$$E_{n\varepsilon} = E_{1,1}^{\text{F-a}} + E_{\text{vib}}(\nu''=0) + \hbar\omega \qquad (25)$$

and μ_{n1} is the electronic transition dipole vector. The semiclassical analogue of this expression can be evaluated using the classical FC principle and a semiclassical Wigner representation of the $\nu'' = 0$ vibrational wave function of the ground electronic state[85]

$$\sigma_{n\varepsilon,10}(\hbar\omega) \approx$$

$$\frac{4\pi^2}{3\hbar c}\hbar\omega \int dQ\, dP_Q\, P^{(1)}(Q, P_Q)[\mu_{n1}]^2\, \delta(H_{n\varepsilon}(Q, P_Q) - E_{n\varepsilon}) \quad (26)$$

where $\hbar\omega$ is the photon energy, and $H_{n\varepsilon}(Q,P_Q)$ is the classical Hamiltonian for the continuum level ε of the nth electronic state, which can be written as[86]

$$H_{n\varepsilon}(Q, P_Q) = \frac{P_Q^2}{2\mu_{\text{HBr}}} + E_{n,n}^{\text{F-a}}(r(Q)) \qquad (27)$$

where μ_{HBr} is the reduced mass of HBr, and $r(Q)$ is the H—Br internuclear distance. The distribution of the normal mode coordinate Q and its conjugate momentum P_Q in the $\nu'' = 0$ vibrational level of the ground electronic state is chosen as the semiclassical Wigner distribution:

$$P^{(1)}(Q, P_Q) = (\pi\hbar)^{-1} \exp\left[-\frac{Q^2}{2s^2} - \frac{2s^2 P_Q^2}{\hbar}\right] \qquad (28)$$

where s is the standard deviation of the normal mode coordinate distribution. This distribution is sampled by the Monte Carlo method with the Box—Muller algorithm.[87]

To evaluate the excited-state potential functions in eq 27, the function $r(Q)$ must be constructed. For this purpose, each value of the displacement δQ of the Q coordinate obtained in the sampling is projected onto the vibrational normal mode vector, the mass scaling is removed, the resulting set of Cartesian coordinates of the H and Br atoms is added to the ground-state equilibrium Cartesian coordinates, and the result is transformed to the internuclear distance r:

$$q_{\kappa i} = L_{\kappa i}\, \delta Q, \qquad \kappa = x, y, z, \quad i = \text{H, Br} \qquad (29)$$

$$x_{\kappa i} = x_{\kappa i,e} + q_{\kappa i}\sqrt{\frac{\mu_{\text{HBr}}}{m_i}}, \qquad \kappa = x, y, z, \; i = \text{H, Br} \quad (30)$$

$$r(Q) = \sqrt{\sum_{\kappa}(x_{\kappa\text{Br}} - x_{\kappa\text{H}})^2}, \qquad \kappa = x, y, z \qquad (31)$$

In eqs 29–31, **L** is the unitless, normalized vibrational normal mode vector obtained from diagonalization and subsequent orthogonalization of the eigenvectors of the Hessian matrix in mass-weighted Cartesian coordinates, **x** is a vector of Cartesian coordinates, and m_i are the atomic masses. The delta function in eq 26 is represented as

$$\delta(H_{n\varepsilon}(Q, P_Q) - E_{n\varepsilon}) = \lim_{\Delta E \to 0}(1/\Delta E)\, \Theta(\Delta E + H_{n\varepsilon}(Q, P_Q) -$$

$$E_{n\varepsilon})\, \Theta(\Delta E - H_{n\varepsilon}(Q, P_Q) + E_{n\varepsilon}) \quad (32)$$

where Θ is Heaviside's step function. Accurate cross sections have been obtained here using a prelimit value of 0.01 eV for ΔE.

2.4. Non-Born–Oppenheimer Semiclassical Trajectory Methods. The reaction dynamics of chemical processes where nonadiabatic or non-BO effects are important can be studied using semiclassical trajectory methods, also called non-BO

molecular dynamics methods. Recent reviews of the non-BO methods used here have been reported elsewhere.[88,89] In these methods, an ensemble (swarm) of trajectories that mimics the finite width of a quantum-mechanical wave packet is used to simulate the nuclear motion. The nuclear trajectories are propagated independently by solving Hamilton's equations of motion, and the electronic quantum-mechanical density matrix **ρ** is propagated along with the trajectory by solving the time-dependent Schrödinger equation. The different independent-trajectory non-BO methods differ in the way they treat the coupling between the electronic and the nuclear motions. The methods used in the present work are of the so-called trajectory surface hopping and decay-of-mixing types, which are detailed next.

In trajectory surface hopping (TSH) methods, the forces acting on the nuclei are determined by a single electronic potential surface except at instantaneous surface switches (also called hops) at which the electronic state changes. At small time intervals along the trajectory a hopping probability is calculated and compared with a random number to decide whether a hop will take place. One of the prescriptions that has been used to compute the hopping probability is the molecular dynamics with quantum transitions method of Tully, which we call Tully's fewest-switches (TFS) method.[90] The TFS method is intended to achieve self-consistency, in an ensemble-average sense, between the number of trajectories that are propagated in each electronic state and the electronic state populations. However, it has been shown that the existence of frustrated hops, that is, hops that are called for by the algorithm but that cannot take place due to insufficient kinetic energy along the hopping vector, spoil the self-consistency of the TFS method. Frustrated hops can be caused by various physical effects, such as when the system attempts to tunnel into a classically forbidden region, and they can also reflect an incorrect treatment of electronic decoherence. The fewest-switches with time-uncertainty (FSTU) method[91] treats the frustrated hops related to nonclassical tunneling by allowing the system to hop at a different time than called for by the hopping algorithm, but within the bounds imposed by the time-energy Heisenberg uncertainty relation. If a suitable time cannot be found, the "∇V prescription"[92] is used to treat the frustrated surface hopping attempt. This prescription does not completely solve the problem of frustrated hops since it does not treat frustrated hops related to electronic decoherence. In a recent improvement, this issue has been addressed by adding stochastic decoherence (SD) to the FTSU method, giving rise to a method that we call the FSTU/SD method.[93] Recently, decoherence was identified as an important effect in the photodissociation of the Na···FH van der Waals complex, and the FSTU/SD method predicted product branching probabilities and excited-state half-lives in excellent agreement with quantum-mechanical results and was shown to be more accurate than the FSTU method.[93]

In the CSDM semiclassical trajectory method,[94] multistate trajectories are propagated according to a mean-field potential energy surface, and the electronic motion is modified to include decoherence and phenomenological demixing. The CSDM method is designed such that the dynamics is relatively representation independent in regions of strong coupling, and CSDM trajectories tend toward pure electronic states in regions where the coupling is negligible. The CSDM method is more accurate than the previously proposed, less coherent self-consistent decay of mixing (SCDM) method[95] and also has the advantage that it depends least on the representation (adiabatic or diabatic) used to describe the electronic part of the system.[88]
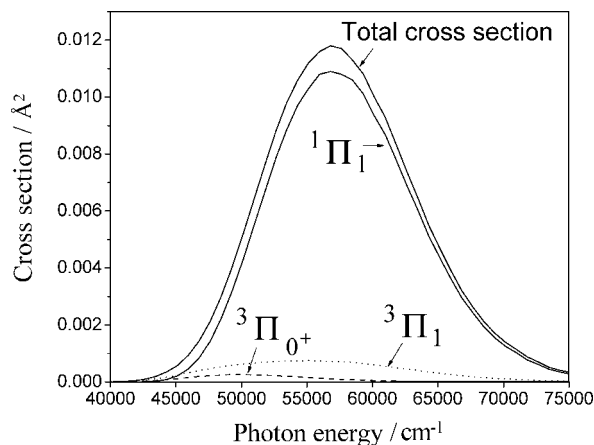
Figure 4. Uncoupled adiabatic total and partial cross sections obtained from fit A. The partial cross section for the $^3\Sigma_1$ state is very small and is not visible in the scale of the figure.

The FSTU and CSDM methods have recently been tested against accurate quantum-mechanical results for a set of two-state atom−diatom reactive scattering systems, which includes systems with varied surface coupling types, from weak interactions to avoided crossings and to conical intersections.[88,89] It was found that the most accurate of the non-BO trajectory methods is CSDM, with an average error of only about 25% in both the adiabatic and the diabatic representations, whereas FSTU led to an average error of about 40% in the adiabatic representation. These errors are on the same order as those for typical single-surface trajectory simulations, suggesting that the treatment of the electronic transitions by the CSDM and FSTU methods does not introduce significant additional error beyond what is already implicit in the classical trajectory approximation.

3. HBr Photodissociation: Nonadiabatic Cross Sections and Branching Fraction

The photodissociation dynamics of HBr has been studied using the CSDM, FSTU, and FSTU/SD semiclassical trajectory methods. The F-adiabatic representation has been employed for all dynamics calculations. All total and partial cross sections are calculated for excitation from the nonrotating $\nu'' = 0$ vibrational level of the ground electronic state. Two kinds of calculations may be carried out in the fully adiabatic representation: (i) fully coupled dynamics and (ii) calculations that neglect the nonadiabatic state coupling. Calculations of type (i) will be called coupled adiabatic, and those of type (ii) will be called uncoupled adiabatic.

The partial absorption cross sections are equal to the uncoupled adiabatic partial photodissociation cross sections for the excited electronic states. They were calculated by sampling the ground-state Wigner distribution of the $\nu'' = 0$ level according to eqs 26–32 using a total of 10^7 samples at 50 photon energies in the range 35 000−75 000 cm^{-1}. The resulting partial and total cross sections are presented in Figure 4. The shape of the total absorption cross section and the position of the maximum ($\sim$56 800 cm^{-1}) are in good agreement with those determined experimentally,[43] but the absolute value at the maximum (0.013 Å^2) is about a factor of 2 lower than experiment (0.027 Å^2). Note that the total cross section found here agrees very well with the theoretical one reported in ref 27, which also differs from experiment by a comparable factor, as pointed out recently.[38] This discrepancy could be due to unconverged transition dipole moments, which are very sensitive to the level of electronic structure theory and to the number of

electronic states included,[34] and/or to experimental inaccuracies. As shown in Figure 4, the only F-adiabatic states with sizable absorption cross sections are $^3\Pi_{0^+}$ (parallel transition) and $^1\Pi_1$ and $^3\Pi_1$ (perpendicular transitions).

According to the discussion of section 2.1, the states that participate in the photodissociation fall into two uncoupled sets of interacting states: $\{X^1\Sigma_{0^+}, ^3\Pi_{0^+}\}$ and $\{^1\Pi_1, ^3\Pi_1, ^3\Sigma_1\}$. The nonadiabatic partial photodissociation cross sections are obtained as the sum of the products of the uncoupled adiabatic partial cross sections and the fraction of semiclassical trajectories in the coupled adiabatic calculations that dissociate to the different electronic states:

$$\sigma_{^3\Pi_{0^+}}^{\text{non-Ad}}(\hbar\omega) = \sigma_{^3\Pi_{0^+}}^{\text{Ad}}(\hbar\omega)\, \Gamma_{^3\Pi_{0^+}}^{^3\Pi_{0^+}}(\hbar\omega) \tag{33}$$

$$\sigma_{X^1\Sigma_{0^+}}^{\text{non-Ad}}(\hbar\omega) = \sigma_{^3\Pi_{0^+}}^{\text{Ad}}(\hbar\omega)\, \Gamma_{X^1\Sigma_{0^+}}^{^3\Pi_{0^+}}(\hbar\omega) \tag{34}$$

$$\sigma_{^1\Pi_1}^{\text{non-Ad}}(\hbar\omega) = \sigma_{^1\Pi_1}^{\text{Ad}}(\hbar\omega)\, \Gamma_{^1\Pi_1}^{^1\Pi_1}(\hbar\omega) + \sigma_{^3\Pi_1}^{\text{Ad}}(\hbar\omega)\, \Gamma_{^1\Pi_1}^{^3\Pi_1}(\hbar\omega) \tag{35}$$

$$\sigma_{^3\Pi_1}^{\text{non-Ad}}(\hbar\omega) = \sigma_{^3\Pi_1}^{\text{Ad}}(\hbar\omega)\, \Gamma_{^3\Pi_1}^{^3\Pi_1}(\hbar\omega) + \sigma_{^1\Pi_1}^{\text{Ad}}(\hbar\omega)\, \Gamma_{^3\Pi_1}^{^1\Pi_1}(\hbar\omega) \tag{36}$$

$$\sigma_{^3\Sigma_1}^{\text{non-Ad}}(\hbar\omega) = \sigma_{^1\Pi_1}^{\text{Ad}}(\hbar\omega)\, \Gamma_{^3\Sigma_1}^{^1\Pi_1}(\hbar\omega) + \sigma_{^3\Pi_1}^{\text{Ad}}(\hbar\omega)\, \Gamma_{^3\Sigma_1}^{^3\Pi_1}(\hbar\omega) \tag{37}$$

In these equations, $\Gamma_j^i(\hbar\omega)$ is the fraction of semiclassical trajectories that start out in electronic state i after absorption of a photon and dissociate in electronic state j, at a given photon energy. Note that when i and j are the same state it can be either because the trajectories dissociate adiabatically or because the system ends up dissociating in the initial state i after two or more nonadiabatic state switches.

The semiclassical trajectory calculations were carried out at the same 50 photon energies included in the importance sampling used to determine the absorption cross sections. The number of trajectories run at a particular energy is equal to the number of accepted Monte Carlo samples at that energy. The initial integration time step chosen was 1 fs, and the trajectories were considered finished after they had been propagated for 50 fs. The integration was carried out using the Bulirsch−Stoer integrator[87] with polynomial extrapolation, with a tolerance parameter ε_{BS} equal to 10^{-9}. A specialized integration scheme[79] that ensures an accurate determination of hopping probabilities in the FSTU and FSTU/SD calculations, and of switching probabilities to the decoherent state when using CSDM, was employed in the present study. The constants C and E_0 in the decay time expression used in CSDM[94] were set to 1 and to 0.1 hartree, respectively.

The nonadiabatic cross sections were found to be similar for the three methods employed, as shown in Table 1 for 10 photon energies in the range where the absorption cross section is sizable. This was to be expected given the good accuracy that has been found for FSTU and CSDM in the adiabatic representation for a number of model atom−diatom systems.[88,89] The number of trajectories run at some representatives photon energies, starting in the $^3\Pi_1$ state and in the $^1\Pi_1$ state, respectively, are as follows: at 43 500 cm^{-1} (close to the maximum branching fraction, see below), 56 000 and 2000; at 58 000 cm^{-1} (about the location of the maximum in total cross section), 30 000 and 80 000; and at 70 000 cm^{-1}, 700 and 2000. Recall that the total number of Monte Carlo samples used to generate the initial conditions is 10^7, and the total number of

Photodissociation of HBr

J. Phys. Chem. A, Vol. 112, No. 25, 2008 **5763**

TABLE 1: Comparison of Nonadiabatic Cross Sections (in Å^{-2}) Obtained with CSDM, FSTU, and FSTU/SD at 10 Selected Photon Energies (in cm^{-1})^a

photon energy	CSDM			FSTU			FSTU/SD		
	$^3\Pi_1$	$^1\Pi_1$	$^3\Sigma_1$	$^3\Pi_1$	$^1\Pi_1$	$^3\Sigma_1$	$^3\Pi_1$	$^1\Pi_1$	$^3\Sigma_1$
38 450	$(3.9 \pm 0.0) \times 10^{-7}$	$(2.0 \pm 1.4) \times 10^{-9}$	0.0	$(3.8 \pm 0.0) \times 10^{-7}$	$(7.9 \pm 3.0) \times 10^{-7}$	0.0	$(3.9 \pm 0.0) \times 10^{-7}$	$(3.9 \pm 1.9) \times 10^{-7}$	0.0
42 620	$(6.3 \pm 2.0) \times 10^{-5}$	$(9.5 \pm 0.4) \times 10^{-6}$	$(5.6 \pm 1.2) \times 10^{-6}$	$(6.3 \pm 2.0) \times 10^{-5}$	$(9.8 \pm 0.4) \times 10^{-5}$	$(3.1 \pm 0.9) \times 10^{-6}$	$(6.3 \pm 2.0) \times 10^{-5}$	$(9.7 \pm 0.4) \times 10^{-5}$	$(4.8 \pm 1.1) \times 10^{-6}$
46 790	$(4.1 \pm 0.1) \times 10^{-4}$	$(8.0 \pm 0.1) \times 10^{-4}$	$(5.4 \pm 0.2) \times 10^{-5}$	$(4.1 \pm 0.1) \times 10^{-4}$	$(8.0 \pm 0.1) \times 10^{-4}$	$(4.6 \pm 0.2) \times 10^{-5}$	$(4.1 \pm 0.1) \times 10^{-4}$	$(7.9 \pm 0.1) \times 10^{-4}$	$(6.0 \pm 0.3) \times 10^{-5}$
50 960	$(7.9 \pm 0.1) \times 10^{-4}$	$(4.9 \pm 0.1) \times 10^{-4}$	$(4.8 \pm 0.2) \times 10^{-4}$	$(8.1 \pm 0.1) \times 10^{-4}$	$(4.9 \pm 0.1) \times 10^{-4}$	$(4.4 \pm 0.2) \times 10^{-4}$	$(8.2 \pm 0.1) \times 10^{-4}$	$(4.8 \pm 0.1) \times 10^{-4}$	$(4.9 \pm 0.2) \times 10^{-4}$
55 130	$(1.1 \pm 0.0) \times 10^{-3}$	$(8.8 \pm 0.2) \times 10^{-3}$	$(1.1 \pm 0.0) \times 10^{-3}$	$(1.1 \pm 0.0) \times 10^{-3}$	$(8.9 \pm 0.2) \times 10^{-3}$	$(1.1 \pm 0.0) \times 10^{-3}$	$(1.1 \pm 0.0) \times 10^{-3}$	$(8.8 \pm 0.2) \times 10^{-3}$	$(1.1 \pm 0.1) \times 10^{-3}$
59 300	$(1.0 \pm 0.0) \times 10^{-3}$	$(8.4 \pm 0.3) \times 10^{-3}$	$(1.3 \pm 0.1) \times 10^{-3}$	$(1.0 \pm 0.0) \times 10^{-3}$	$(8.4 \pm 0.3) \times 10^{-3}$	$(1.3 \pm 0.1) \times 10^{-3}$	$(1.0 \pm 0.0) \times 10^{-3}$	$(8.3 \pm 0.3) \times 10^{-3}$	$(1.3 \pm 0.1) \times 10^{-3}$
63 470	$(6.3 \pm 0.2) \times 10^{-4}$	$(4.9 \pm 0.3) \times 10^{-3}$	$(8.8 \pm 1.0) \times 10^{-3}$	$(6.5 \pm 0.2) \times 10^{-4}$	$(4.9 \pm 0.3) \times 10^{-3}$	$(8.9 \pm 1.5) \times 10^{-3}$	$(6.4 \pm 0.2) \times 10^{-4}$	$(4.8 \pm 0.3) \times 10^{-3}$	$(9.3 \pm 1.3) \times 10^{-3}$
67 640	$(2.9 \pm 0.2) \times 10^{-4}$	$(1.9 \pm 0.3) \times 10^{-3}$	$(4.2 \pm 1.1) \times 10^{-3}$	$(2.9 \pm 0.2) \times 10^{-4}$	$(1.9 \pm 0.2) \times 10^{-3}$	$(4.2 \pm 1.3) \times 10^{-3}$	$(2.8 \pm 0.2) \times 10^{-4}$	$(1.9 \pm 0.2) \times 10^{-3}$	$(4.3 \pm 1.3) \times 10^{-3}$
71 810	$(1.2 \pm 0.1) \times 10^{-4}$	$(5.8 \pm 1.3) \times 10^{-4}$	$(1.5 \pm 0.7) \times 10^{-4}$	$(1.1 \pm 0.0) \times 10^{-4}$	$(6.1 \pm 1.4) \times 10^{-4}$	$(1.3 \pm 1.3) \times 10^{-4}$	$(1.1 \pm 0.1) \times 10^{-4}$	$(5.9 \pm 0.1) \times 10^{-4}$	$(1.5 \pm 1.1) \times 10^{-4}$
75 980	$(4.0 \pm 0.9) \times 10^{-5}$	$(1.4 \pm 0.1) \times 10^{-4}$	$(5.7 \pm 0.6) \times 10^{-5}$	$(3.8 \pm 1.3) \times 10^{-5}$	$(1.4 \pm 0.8) \times 10^{-4}$	$(5.2 \pm 0.8) \times 10^{-5}$	$(3.1 \pm 3.1) \times 10^{-5}$	$(1.7 \pm 0.1) \times 10^{-4}$	$(3.5 \pm 1.3) \times 10^{-5}$

^{a} Statistical errors correspond to one standard deviation.

nonadiabatic trajectories run is about 4×10^6. The statistical error in the nonadiabatic cross sections was computed as the Monte Carlo error (one standard deviation)[96] in the fraction of trajectories that dissociate in each of the F-adiabatic electronic states:

$$\frac{\Delta\sigma_{1\Pi_1}^{non\text{-}Ad}(\hbar\omega)}{\sigma_{1\Pi_1}^{non\text{-}Ad}(\hbar\omega)} = \left(\frac{N_T^{1\Pi_1}(\hbar\omega) - N_{1\Pi_1}^{1\Pi_1}(\hbar\omega)}{N_{1\Pi_1}^{1\Pi_1}(\hbar\omega)\,N_T^{1\Pi_1}(\hbar\omega)} + \frac{N_T^{3\Pi_1}(\hbar\omega) - N_{1\Pi_1}^{3\Pi_1}(\hbar\omega)}{N_{1\Pi_1}^{3\Pi_1}(\hbar\omega)\,N_T^{3\Pi_1}(\hbar\omega)}\right)^{1/2} \quad (38)$$

$$\frac{\Delta\sigma_{3\Pi_1}^{non\text{-}Ad}(\hbar\omega)}{\sigma_{3\Pi_1}^{non\text{-}Ad}(\hbar\omega)} = \left(\frac{N_T^{1\Pi_1}(\hbar\omega) - N_{3\Pi_1}^{1\Pi_1}(\hbar\omega)}{N_{3\Pi_1}^{1\Pi_1}(\hbar\omega)\,N_T^{1\Pi_1}(\hbar\omega)} + \frac{N_T^{3\Pi_1}(\hbar\omega) - N_{3\Pi_1}^{3\Pi_1}(\hbar\omega)}{N_{3\Pi_1}^{3\Pi_1}(\hbar\omega)\,N_T^{3\Pi_1}(\hbar\omega)}\right)^{1/2} \quad (39)$$

$$\frac{\Delta\sigma_{3\Sigma_1}^{non\text{-}Ad}(\hbar\omega)}{\sigma_{3\Sigma_1}^{non\text{-}Ad}(\hbar\omega)} = \left(\frac{N_T^{1\Pi_1}(\hbar\omega) - N_{3\Sigma_1}^{1\Pi_1}(\hbar\omega)}{N_{3\Sigma_1}^{1\Pi_1}(\hbar\omega)\,N_T^{1\Pi_1}(\hbar\omega)} + \frac{N_T^{3\Pi_1}(\hbar\omega) - N_{3\Sigma_1}^{3\Pi_1}(\hbar\omega)}{N_{3\Sigma_1}^{3\Pi_1}(\hbar\omega)\,N_T^{3\Pi_1}(\hbar\omega)}\right)^{1/2} \quad (40)$$

where $N_T^i(\hbar\omega)$ is the total number of trajectories starting in state $i = {}^3\Pi_1$ or $^1\Pi_1$, run at a particular photon energy, and $N_j^i(\hbar\omega)$ is the number of trajectories that start out in state i and dissociate in state j (compare with eqs 33–37). The results presented in Table 1 show that the three methods agree within statistical uncertainty for trajectories that dissociate in the $^3\Pi_1$ and $^1\Pi_1$ states. Interestingly, the FSTU/SD method improves the FSTU nonadiabatic cross sections for the $^3\Sigma_1$ state in a statistically significant way, in the sense that the FSTU/SD results are closer to the presumably more accurate[89] CSDM results. The agreement improves especially at low photon energies. This can be understood noting that the FSTU/SD method may affect the dynamics of the trajectories that experience more than one surface hop.[93] The fraction of such trajectories (relative to the total number of hopping trajectories) is significant, oscillating between 30% and 15% at the lowest and the highest photon energies, respectively, for trajectories started in the $^3\Pi_1$ state, and between 50% and 15% for trajectories started in the $^1\Pi_1$ state. The FSTU/SD method has also been found to perform better than FSTU for photodissociation of the Na···FH van der Waals complex.[93]

The results of the CSDM calculations are presented in Figure 5. Trajectories were started in the $^1\Pi_1$ and $^3\Pi_1$ adiabatic states, whereas it was assumed that dissociation on the $^3\Pi_{0^+}$ state proceeds adiabatically despite the nonzero nonadiabatic coupling between this state and the ground electronic state. Exploratory calculations showed that the transition probability from $^3\Pi_{0^+}$ to $X^1\Sigma_{0^+}$ does not exceed a few percent. This can be understood from the large vertical separation between these states in the region of their maximum nonadiabatic coupling near 2.7 Å (see Figure 2). One observes that the $^3\Sigma_1$ state has a sizable nonadiabatic cross section, whereas it has a negligible adiabatic cross section as seen in Figure 4. According to eq 37, the $^3\Sigma_1$ state can be accessed by nonadiabatic transitions after photon absorption from the $^1\Pi_1$ state or from the $^3\Pi_1$ state. Examination
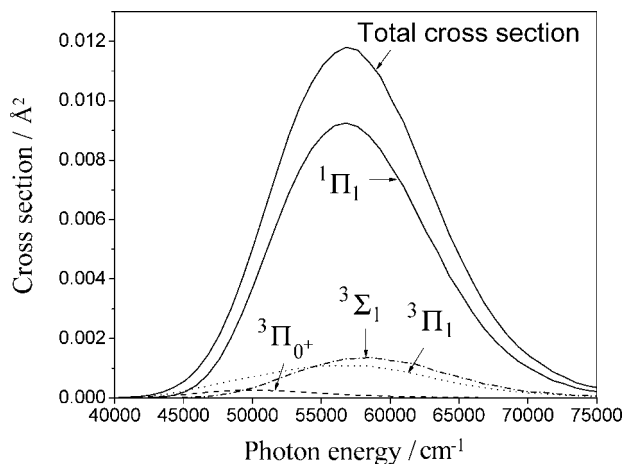
Figure 5. Nonadiabatic total and partial cross sections obtained in coupled adiabatic calculations with the CSDM semiclassical trajectory method using fit A.

of the theoretical results shows that essentially all of the dissociation flux in the $^3\Sigma_1$ state comes from the $^1\Pi_1$ state, as could be expected, since $^1\Pi_1$ is energetically closer to $^3\Sigma_1$ than $^3\Pi_1$ is (see Figure 1), $^1\Pi_1$ has a larger adiabatic absorption cross section, and its nonadiabatic coupling with $^3\Sigma_1$ is larger than that between $^3\Pi_1$ and $^3\Sigma_1$. A surprising result is that the nonadiabatic cross sections for $^1\Pi_1$ and $^3\Pi_1$ are quite similar to the uncoupled adiabatic cross sections. This disagrees both with the results of ref 27 and with the experiment;[25] the latter yields a transition probability from $^1\Pi_1$ to $^3\Pi_1$ at a photon energy of 51 600 cm^{-1} of about 80% and therefore predicts significantly more formation of $^3\Pi_1$ and less formation of $^1\Pi_1$.

To shed light on the factors that cause this discrepancy, we have refitted the ab initio adiabatic and diabatic energies and the diabatic couplings. For the energies, five-term even-tempered sums of exponentials have been employed

$$f(r) = \sum_{i=0}^{5} c_i \exp(-\alpha\beta^i(r - r_0)) + f\Delta E_{SO,Br} \quad (41)$$

and an analogous expression with nine terms has been used for the diabatic couplings:

$$g(r) = \sum_{i=0}^{8} c_i \exp(-\alpha\beta^i(r - r_0)) \quad (42)$$

For the adiabatic and diabatic energies, the even-tempered coefficients α and β have been kept fixed at 1.3 Å^{-1} and 1.5, respectively, and r_0 has been set to 1.4 Å. Therefore, the fits in eqs 41 and 42 are linear fits. These simple functional forms with fixed parameters were chosen to obtain a good match with the ab initio energies at not too long distances (up to about 3.0 Å), and to explore the sensitivity of the nonadiabatic couplings to small energetic differences between the different electronic states in the long-range region. The parameters of the energy fits are given in Tables S6 (diabatic) and S8 (adiabatic) of Supporting Information. For the diabatic couplings, the same values of α and β as for the energies have been chosen, and r_0 has been chosen equal to 1.0 Å. The parameters of the diabatic coupling fits are given in Table S7 of Supporting Information. As stated above, these fits differ significantly from fit A only for distances longer than about 3.0 Å, where they deviate by a few millielectronvolts from the ab initio data. These differences give rise to a much increased nonadiabatic coupling between the $^1\Pi_1$ and $^3\Pi_1$ states. The remaining features of the potentials,

as well as the nonadiabatic couplings between the other electronic states, are similar to those of fit A. Nevertheless, since the nonadiabatic couplings are very important for the dynamics, all of them were refitted using the same expression as for fit A. In this case, the full expression in eq 6 was fitted in a single step to

$$d_{ij}(r) = \sum_{K=1}^{N} c_{ij,K} \exp(-\alpha_{ij}\beta_{ij}^K(r - r_{ij,K})^2) \quad (43)$$

where now $N = 5$ for the $X^1\Sigma_{0^+}-^3\Pi_{0^+}$, $^1\Pi_1-^3\Sigma_1$, and $^3\Pi_1-^3\Sigma_1$ nonadiabatic couplings, and $N = 9$ for the $^1\Pi_1-^3\Pi_1$ one. The parameters of these fits are given in Table S9 of Supporting Information. The new set of fitted adiabatic energies, diabatic energies and couplings, and nonadiabatic couplings, will be called fit B. The nonadiabatic coupling curves are shown in Figure 6. Comparing with Figure 2, it is clear that the only significant difference is a much larger nonadiabatic coupling between the $^1\Pi_1$ and $^3\Pi_1$ states, with a maximum of close to 2.0 Å^{-1} for an internuclear distance of about 3.7 Å.

A comparison of the F-diabatic energies obtained in fits A and B in the long-range region with the ab initio data is presented in Figure 7. In Figure 7A one observes the high accuracy of fit A in reproducing the ab initio data, in particular, the shallow minima with depths between 4 and 6 meV located in the region of r from 3.7 to 4.3 Å. Comparable accuracy is achieved for the diabatic couplings and for the adiabatic energies, and the results are not shown here. In contrast, the fit B curves in Figure 7B deviate considerably from the F-diabatic energies in this region, to the extent that the minima either disappear or are extremely shallow, and some of the curves cross. These features of fit B lead to a large nonadiabatic coupling between the $^1\Pi_1$ and $^3\Pi_1$ states, as mentioned above. As seen in eq 6, nonadiabatic couplings are large when some of the nuclear derivatives of the diabatic energies and/or couplings are large, when both adiabatic states involved have relatively large coefficients for the given diabatic state or states, or when the difference between the adiabatic energies is small. Analysis of the contributions to the nonadiabatic coupling between the $^1\Pi_1$ and $^3\Pi_1$ states shows that, at long range, for fit A the coefficients of the eigenvectors of these F-adiabatic states in eq 6 are all close to 1 or 0. However, for fit B the coefficients relative to $H_{4,4}^{F-d}(r)$ are both quite different from 1 or 0. This is probably related to the crossing between the diabatic states observed in Figure 7B. As a result, and since the derivative of $H_{4,4}^{F-d}(r)$ is also sizable in this region (although it is comparable

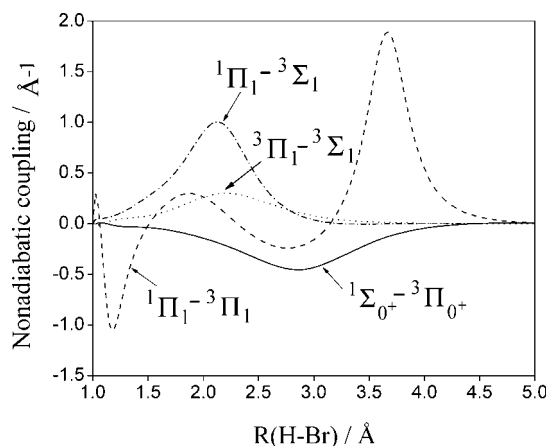**Figure 6.** Nonadiabatic coupling curves for the HBr molecule obtained in fit B.

Photodissociation of HBr

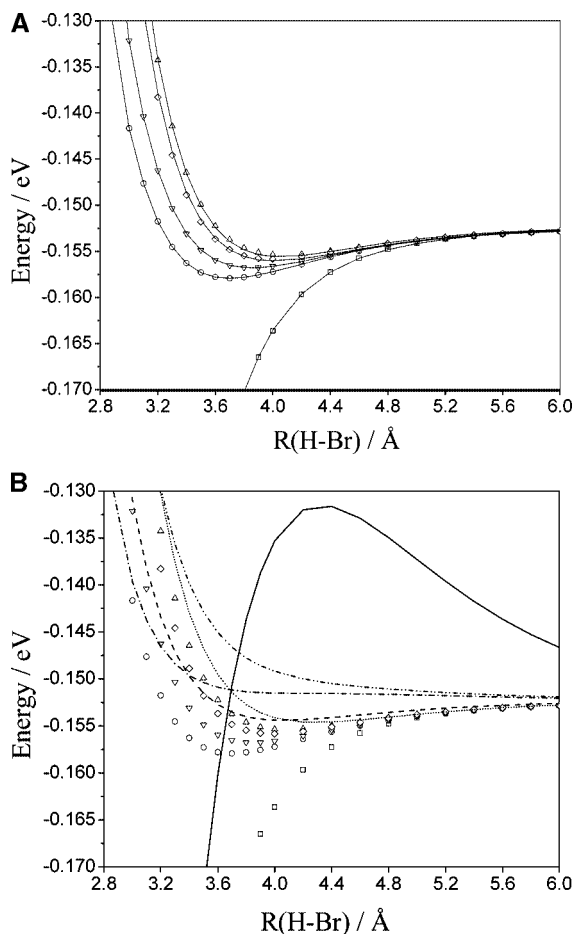*J. Phys. Chem. A, Vol. 112, No. 25, 2008* **5765**

Figure 7. Comparison between the long-range energies obtained in fit A (A) and fit B (B) and the ab initio F-diabatic energies for the states that correlate with the lower fine-structure level of bromine. The symbols represent ab initio data and the lines represent the fitted energies. The states plotted in part A are $H_{1,1}^{\text{F-d}}(r)$ (squares), $H_{2,2}^{\text{F-d}}(r)$ (circles), $H_{4,4}^{\text{F-d}}(r)$ (triangles), $H_{6,6}^{\text{F-d}}(r)$ (inverted triangles), and $H_{12,12}^{\text{F-d}}(r)$ (rhombi). The state correspondence in part B is $H_{1,1}^{\text{F-d}}(r)$ (squares and solid line), $H_{2,2}^{\text{F-d}}(r)$ (circles and dash−dot line), $H_{4,4}^{\text{F-d}}(r)$ (triangles and dot line), $H_{6,6}^{\text{F-d}}(r)$ (inverted triangles and dash line), and $H_{12,12}^{\text{F-d}}(r)$ (rhombi and dash−dot−dot line).

for fits A and B), for fit A the nonadiabatic coupling is close to 0, whereas it has a large magnitude for fit B.

A new set of CSDM calculations was carried out with fit B with the transition dipole moments from fit A, and the total and partial cross sections obtained are presented in Figure 8. In this case, the partial cross sections for $^1\Pi_1$ and $^3\Pi_1$ are in better agreement with those reported in the literature, although the nonadiabatic redistribution of flux from $^1\Pi_1$ to $^3\Pi_1$ is still somewhat underestimated. The remaining cross sections are essentially the same as those in Figure 5. Thus, despite the fact that fit B is less accurate than fit A, it seems to describe better the nonadiabatic transition between the $^1\Pi_1$ and $^3\Pi_1$ F-adiabatic states, which are predicted to take place predominantly at long range in a region where these states are energetically very close. The accurate prediction of interaction energies in this region, where weak van der Waals interactions must be considered, is particularly difficult and would require additional high-level corrections, such as saturating the one-electron basis set, treating electronic correlation using coupled-cluster-type methods, systematically including connected triple excitations, and taking into account basis set superposition error (BSSE) effects.[97] That level of treatment is beyond the scope of the present study, and we just note that the redistribution of the dissociation flux to
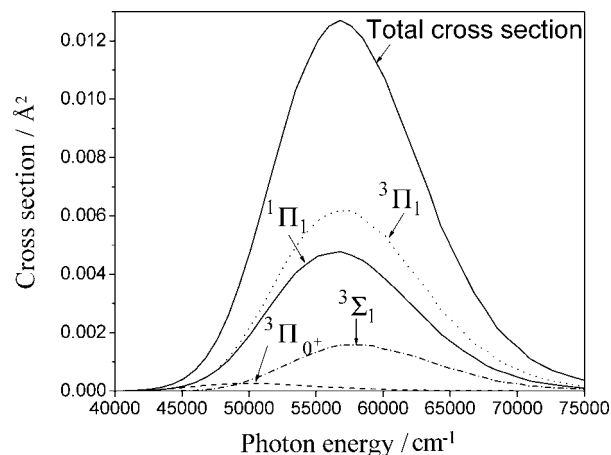

Figure 8. Nonadiabatic total and partial cross sections obtained in coupled adiabatic calculations with the CSDM semiclassical trajectory method using fit B.
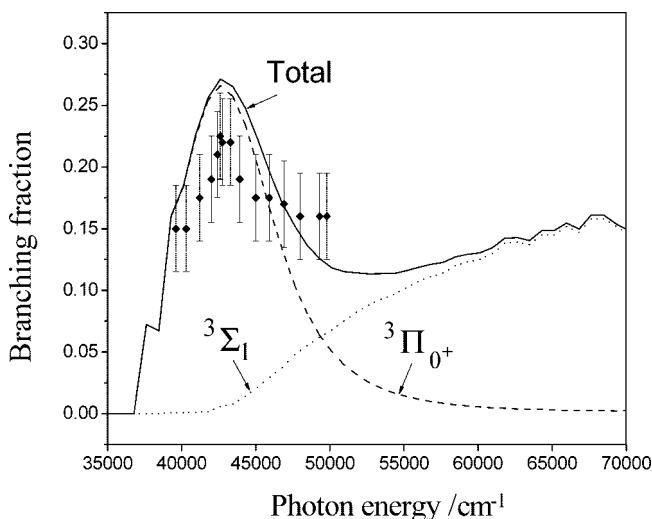

Figure 9. Branching fraction to the higher fine-structure level of bromine obtained in coupled adiabatic calculations with the CSDM semiclassical trajectory method using fit A. The experimental measurements[24] (symbols with error bars), and the theoretical branching fraction with the contributions from the $^3\Sigma_1$ and $^3\Pi_{0^+}$ F-adiabatic states, are shown in the figure.

the $^1\Pi_1$ and $^3\Pi_1$ states correlating with the lower fine-structure level of bromine is very sensitive to the long-range region of the potentials.

A very important dynamic property for systems in which spin−orbit effects are sizable is the branching fraction to the higher fine-structure level of separated fragments. For HBr, the nonadiabatic photodissociation cross sections for the $^1\Pi_1$, $^3\Pi_1$, and $^3\Sigma_1$ states, and the uncoupled adiabatic cross sections for the $^3\Pi_{0^+}$ state, allow one to determine the branching fraction to $H(^2S) + Br(^2P_{1/2})$ as

$$\Gamma(\hbar\omega) = \frac{\sigma_{^3\Pi_{0^+}}^{\text{Ad}}(\hbar\omega) + \sigma_{^3\Sigma_1}^{\text{non-Ad}}(\hbar\omega)}{\sigma_{^1\Pi_1}^{\text{non-Ad}}(\hbar\omega) + \sigma_{^3\Pi_1}^{\text{non-Ad}}(\hbar\omega) + \sigma_{^3\Pi_{0^+}}^{\text{Ad}}(\hbar\omega) + \sigma_{^3\Sigma_1}^{\text{non-Ad}}(\hbar\omega)} \quad (44)$$
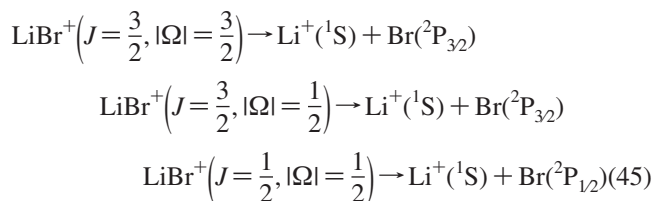
The resulting branching fraction as a function of photon energy computed with CSDM using fit A is compared with experiment in Figure 9. The agreement is quite good in the range where experimental results have been reported; in particular, the peak at about 43 000 cm^{-1} is well reproduced,

although the predicted branching fraction is slightly larger than the experimental one. Note that in the wave packet calculations of ref 27 the theoretical maximum in the branching fraction is at somewhat lower energies and the shape of the curve is flatter than in the experiment and the present calculations. At this photon energy, the absorption cross sections are very small, as seen in Figures 4 and 5, and any inaccuracies in the potentials or transition dipole moments could cause a difference of this order. We attribute the better agreement obtained in the present study to the larger $X^1\Sigma_{0^+} \rightarrow {}^3\Pi_{0^+}$ transition dipole moment obtained, which is responsible for the maximum in the branching fraction as observed in Figure 9. This behavior is probably due to the inclusion of the triplet spin-free permanent and transition dipole moments in the transformation of eq 16. It is likely that the authors of ref 27 only included the largest contribution to the spin-coupled transition dipole moments, which is that from the singlet spin-free permanent and transition dipole moments.

It is interesting that a dynamic property such as the branching fraction of HBr is controlled to a large extent by the partial absorption cross sections to the relevant excited states. The level of control is even larger in photodissociation of HI, for which the uncoupled adiabatic partial absorption cross sections almost completely determine the branching fraction because nonadiabatic effects have been found to be negligible.[34,46] For both HI[34] and CH$_3$I,[98] it has been predicted that the branching fraction can be increased significantly by vibrational excitation in the ground electronic state, if the photon wavelength is selected so that the excited-state potentials that correlate adiabatically with the higher fine-structure level of products strongly dominate the total absorption cross sections.

4. Spin-Coupled Potential Curves for LiBr$^+$

The method used here to obtain spin-coupled potential and dipole moment curves for HBr has previously been formulated explicitly only for even-electron systems.[76] However, many of the benchmark systems for the study of spin−orbit effects on reaction dynamics are odd-electron systems containing an open-shell atom in a degenerate electronic state (e.g., X(^{2}P) where X is a halogen) that reacts with a closed-shell molecule (e.g., H$_2$($\tilde{X}$ $^1\Sigma_g^+$), HX($\tilde{X}^1\Sigma^+$)). To show that the method can be applied to both even- and odd-electron systems, we have studied a model odd-electron system with a single unpaired electron, namely, the LiBr$^+$ diatomic. To our knowledge there is no experimental data for LiBr$^+$ to which one can compare. However, calculations of the potential energies that include an ab initio distance-dependent SOC can be compared to calculations at the same level of electronic structure but assuming a constant SOC. At internuclear distances where the interaction between the atoms is not negligible, the ^{2}P state of bromine splits under the influence of the spin-free electronic Hamiltonian into a $^2\Sigma$ and a $^2\Pi$ curve. Introducing the spin−orbit operator in the Hamiltonian gives rise to three doubly degenerate spin-coupled states (Kramers doublets) in the molecular region, two with $|\Omega| = 1/2$ and one with $|\Omega| = 3/2$. The spin-coupled electronic states are labeled according to the value of the total electronic angular momentum in the dissociation limit (equal to that of the bromine atom) and of $|\Omega|$. The correlations of these molecular states with the atomic asymptotic states are

$$LiBr^+\left(J=\frac{3}{2}, |\Omega|=\frac{3}{2}\right) \rightarrow Li^+(^1S) + Br(^2P_{3/2})$$

$$LiBr^+\left(J=\frac{3}{2}, |\Omega|=\frac{1}{2}\right) \rightarrow Li^+(^1S) + Br(^2P_{3/2})$$

$$LiBr^+\left(J=\frac{1}{2}, |\Omega|=\frac{1}{2}\right) \rightarrow Li^+(^1S) + Br(^2P_{1/2}) \quad (45)$$

The present treatment is designed for energies where the asymptotic states of eq 45 are the only energetically accessible ones.

The spin-free potential energy curves of the $^2\Sigma$ and $^2\Pi$ electronic states are obtained as follows. First, SA-CASSCF calculations are performed with an active space of five electrons in three orbitals, choosing an equal weight for each of the three substates included in the average (one substate for $^2\Sigma$ and two substates for $^2\Pi$). The MOs obtained are subsequently used in CISD calculations that include all single and double excitations from the highest three MOs to the space of virtual MOs, keeping the rest of the MOs frozen. The spin−orbit interaction has been computed from the CISD eigenstates including the full spin−orbit part of the Breit−Pauli Hamiltonian.[99] The correlation-consistent aug-cc-pVTZ basis set[52,100,101] has been employed in all the calculations, which were performed with the GAMESS program.[102]

The procedure used to construct spin-coupled potential curves from the spin-free electronic states and assuming constant spin−orbit interaction is analogous to that used for HBr. Briefly, the valence diabatic matrix for LiBr$^+$ is a 6 × 6 diagonal matrix with the CISD energies as its diagonal elements

$$H_{\alpha\alpha'}^{Val}(r) = E_\alpha(r)\delta_{\alpha\alpha'}, \quad 1 \le \alpha \le 6 \quad (46)$$

where α labels the V-diabatic substates and r is the Li−Br internuclear distance. The zero of energy is chosen as the energy of the six degenerate V-diabatic substates without SOC in the dissociation limit. The transformation matrix to the F-diabatic representation is denoted $\mathbf{C}^{(6)}$

$$\mathbf{H}^{SO,F-d}(\infty) = \mathbf{C}^{(6)\dagger}\mathbf{H}^{SO,Val}(\infty)\mathbf{C}^{(6)} \quad (47)$$

where $\mathbf{H}^{SO,F-d}(\infty)$ is a diagonal matrix with four elements equal to the energy of the Br($^2P_{3/2}$) fine-structure level, $-\Delta E_{SO,Br}/3$, and two elements equal to the energy of the Br($^2P_{1/2}$) level, $2\Delta E_{SO,Br}/3$, with $\Delta E_{SO,Br}$ the CISD fine-structure splitting of the bromine atom (3243 cm^{-1}). The F-diabatic potential energy matrix is obtained from

$$\mathbf{H}^{F-d}(r) = \mathbf{C}^{(6)\dagger}\mathbf{H}^{Val}(r)\mathbf{C}^{(6)} + \mathbf{H}^{SO,F-d}(\infty) \quad (48)$$

Diagonalization of the F-diabatic potential matrix yields the F-adiabatic potential energies.

The spin−orbit matrix and the corresponding transformation to spin-coupled diabatic states for the case of a ^{2}P atom interacting with a closed-shell atom or molecule has been considered by several authors (see, for instance, refs 104 and 105 and references therein). However, for the sake of completeness, the spin−orbit matrix in the V-diabatic representation for LiBr$^+$ is presented in Table 2, and the $\mathbf{C}^{(6)}$ transformation matrix is presented in Table 3 (the analogous matrices for HBr were given in ref 76).

The spin-coupled F-adiabatic potential energy curves obtained from the ab initio calculations including the r-dependent SOC are shown in Figure 10. The three curves all have minima at short internuclear distances, relatively deep for the two lowest curves correlating with Br($^2P_{3/2}$) and rather shallow for the highest curve correlating with Br($^2P_{1/2}$). This behavior contrasts with other cases such as X(^{2}P) + H$_2$ and X(^{2}P) + HX, for which

TABLE 2: Elements of the Matrix of H^{SO} for LiBr$^+$ in the V-Diabatic Representation[a]

	$^2\Sigma$	$^2\bar{\Sigma}$	$^2\Pi_x$	$^2\bar{\Pi}_x$	$^2\Pi_y$	$^2\bar{\Pi}_y$
$^2\Sigma$	0.0	0.0	0.0	λ	0.0	$-\lambda i$
$^2\bar{\Sigma}$	0.0	0.0	$-\lambda$	0.0	$-\lambda i$	0.0
$^2\Pi_x$	0.0	$-\lambda$	0.0	0.0	λi	0.0
$^2\bar{\Pi}_x$	λ	0.0	0.0	0.0	0.0	$-\lambda i$
$^2\Pi_y$	0.0	λi	$-\lambda i$	0.0	0.0	0.0
$^2\bar{\Pi}_y$	λi	0.0	0.0	λi	0.0	0.0

[a] The symbols in the first row and the first column indicate the V-diabatic states. For the nonzero elements of the matrix, λ is defined as $\Delta E_{SO}/3$, where ΔE_{SO} is the spin−orbit fine-structure splitting of bromine, and i denotes $\sqrt{(-1)}$.

TABLE 3: Elements of the $C^{(6)}$ Transformation Matrix of LiBr$^+$ [a]

	$J = 3/2$, $\Omega = 3/2$	$J = 3/2$, $\Omega = -3/2$	$J = 3/2$, $\Omega = 1/2$	$J = 3/2$, $\Omega = -1/2$	$J = 1/2$, $\Omega = 1/2$	$J = 1/2$, $\Omega = -1/2$
$^2\Sigma$	0.0	0.0	$\sqrt{(2/3)}$	0.0	$\sqrt{(1/3)}$	0.0
$^2\bar{\Sigma}$	0.0	0.0	0.0	$\sqrt{(2/3)}$	0.0	$\sqrt{(1/3)}$
$^2\Pi_x$	$\sqrt{(1/2)}$	0.0	0.0	$\sqrt{(1/6)}$	0.0	$-\sqrt{(1/3)}$
$^2\bar{\Pi}_x$	0.0	$-\sqrt{(1/2)}$	$-\sqrt{(1/6)}$	0.0	$\sqrt{(1/3)}$	0.0
$^2\Pi_y$	$\sqrt{(1/2)}i$	0.0	0.0	$-\sqrt{(1/6)}i$	0.0	$\sqrt{(1/3)}i$
$^2\bar{\Pi}_y$	0.0	$\sqrt{(1/2)}i$	$-\sqrt{(1/6)}i$	0.0	$\sqrt{(1/3)}i$	0.0

[a] The symbols in the first column indicate the V-diabatic states, and the symbols above columns 2−7 indicate, for each of the F-diabatic states, the value of the total electronic angular momentum of the bromine atom, J, in the dissociation limit, and the value of its projection on the internuclear axis, Ω. i denotes $\sqrt{(-1)}$.
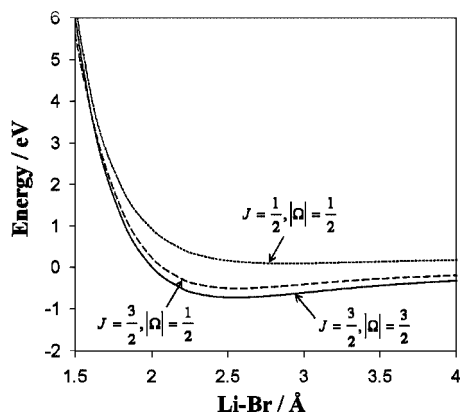
Figure 10. F-adiabatic potential energy curves for the LiBr$^+$ molecule obtained using the ab initio, r-dependent SOC.

attractive interactions are present only at long range, giving rise to van der Waals wells.[103] This difference can be attributed to the ionic character of Li$^+$. The strong interaction of the ionic collision partner with the Br atom makes this a good test case for electronic structure theory. At the resolution discernible in Figure 10, the potential energies obtained using the atomic SOC approximation are not presented graphically. In the range of Li−Br distances from 1.4 to 5.0 Å, the mean unsigned deviation of the curves in Figure 11 from those in Figure 10 is 2.6 meV. This is of the same order as that obtained for the HBr diatomic.[76] Note that the energies of the LiBr$^+$ F-adiabatic states span a wide range, from about −0.7 eV at the lowest minimum to almost 9 eV at 1.4 Å. Thus the mean unsigned deviation is only 0.03% of the range covered. The two unique spin−orbit matrix elements in the V-diabatic representation can be written $\langle\Pi_x|\hat{H}_{SO}|\Pi_y\rangle$ and $\langle\bar{\Pi}_x|\hat{H}_{SO}|\Sigma\rangle$,[104] where the symmetry symbols without a bar over them are associated with an α spin function and the symbol with a bar is associated with a β spin function. The asymptotic value of these matrix elements, 1081 cm^{-1} or

0.134 eV, is equal to one-third of the ab initio fine-structure splitting of bromine. These matrix elements show a maximum variation relative to these asymptotes of about 3 and 14 meV, respectively, which is on the same order as but somewhat larger than the deviations of the potential energies from the ab initio computed ones.

5. Conclusions

The photodissociation of HBr is a computationally tractable process that allows one to test the accuracy of two key simplifications, namely, (i) using distance-independent (atomic) spin−orbit couplings at all internuclear distances to obtain spin-coupled potentials and transition dipole moments and (ii) using semiclassical trajectories to compute the photofragmentation dynamics. Although one can readily use more accurate methods for studying the photodissociation of a diatomic molecule, our goal here is to test methods that are practical for polyatomic photodissociation by applying them to a case where one also has more complete theoretical treatments available.

First, the adiabatic total and partial absorption cross sections were computed by sampling of the $v'' = 0$ vibrational state of the ground electronic state. The resulting total cross sections underestimate the experiment by about a factor of 2 but are in good agreement with wave packet calculations, indicating most probably that there is room for improvement in the transition dipole moments.

The nonadiabatic photodissociation dynamics was studied using one semiclassical trajectory method of the decay-of-mixing type (in particular, CSDM) and two of the surface-hopping type (in particular, FSTU and FSTU/SD). The results are very similar for the three methods, and the predicted branching fractions are in good agreement with experiment. The redistribution of reactive flux between two of the electronic states correlating with the lower fine-structure level of bromine atom was found to depend strongly on the shape of the potential curves at long internuclear distances. The most accurate fits fail to reproduce qualitatively the experimental behavior, suggesting that the long-range potentials should be improved.

The same strategy used to generate potential and transition dipole moment curves for HBr was applied to the LiBr$^+$ odd-electron system, and it was found that using the atomic spin−orbit coupling reproduces the spin-coupled ab initio energies almost quantitatively in the whole range of internuclear distances studied.

The general conclusion of the present study is that for a system such as HBr the same level of accuracy can be attained for the total cross section and the spin−orbit branching fraction by using semiclassical trajectory methods, a semiclassical initial state sample scheme, and a distance-independent spin−orbit coupling as can be attained by using more complicated and expensive quantum-mechanical wave packet methods and a distance-dependent ab initio spin−orbit coupling. This validates the simpler methods for applications involving larger systems.

Supporting Information Available: Parameters of all the fits carried out in the present work. This material is available free of charge via the Internet at http://pubs.acs.org.

5768 *J. Phys. Chem. A, Vol. 112, No. 25, 2008*

Valero et al.

References and Notes

(1) Zhang, J.; Riehn, C. W.; Dulligan, M.; Wittig, C. *J. Chem. Phys.* **1996**, *104*, 7027.

(2) Brown, A.; Balint-Kurti, G. G. *J. Chem. Phys.* **2000**, *113*, 1870.

(3) Brown, A.; Balint-Kurti, G. G. *J. Chem. Phys.* **2000**, *113*, 1879.

(4) Balint-Kurti, G. G.; Orr-Ewing, A. J.; Beswick, J. A.; Brown, A.; Vasyutinskii, O. S. *J. Chem. Phys.* **2002**, *116*, 10760.

(5) Givertz, S. C.; Balint-Kurti, G. G. *J. Chem. Soc., Faraday Trans. 2* **1986**, *82*, 1231.

(6) Matsumi, Y.; Tonokura, K.; Kawasaki, M.; Ibuki, T. *J. Chem. Phys.* **1990**, *93*, 7981.

(7) Alexander, M. H.; Pouilly, B.; Duhoo, T. *J. Chem. Phys.* **1993**, *99*, 1752.

(8) Gersonde, I. H.; Hennig, S.; Gabriel, H. *J. Chem. Phys.* **1994**, *101*, 9558.

(9) Duhoo, T.; Pouilly, B. *J. Chem. Phys.* **1995**, *103*, 182.

(10) Lambert, H. M.; Dagdigian, P. J.; Alexander, M. H. *J. Chem. Phys.* **1998**, *108*, 4460.

(11) Alexander, M. H.; Li, X.; Liyanage, R.; Gordon, R. *J. Chem. Phys.* **1998**, *231*, 331.

(12) Lee, S.; Jung, K.-H. *J. Chem. Phys.* **2000**, *112*, 2810.

(13) Regan, P. M.; Ascenzi, D.; Brown, A.; Balint-Kurti, G. G.; Orr-Ewing, A. J. *J. Chem. Phys.* **2000**, *112*, 10259.

(14) Brown, A.; Balint-Kurti, G. G.; Vasyutinskii, O. S. *J. Phys. Chem. A* **2004**, *108*, 7790.

(15) Grage, M. M. L.; Nyman, G.; Johnson, M. S. *Phys. Chem. Chem. Phys.* **2006**, *8*, 4798.

(16) Magnotta, F.; Nesbitt, D. J.; Leone, S. R. *Chem. Phys. Lett.* **1981**, *80*, 21.

(17) Xu, Z.; Koplitz, B.; Wittig, C. *J. Chem. Phys.* **1987**, *87*, 1062.

(18) Xu, Z.; Koplitz, B.; Wittig, C. *J. Phys. Chem.* **1988**, *92*, 5518.

(19) Chapman, D. A.; Balasubramanian, K.; Lin, S. H. *Chem. Phys.* **1987**, *118*, 333.

(20) Kinugawa, T.; Arikawa, T. *J. Chem. Phys.* **1992**, *96*, 4801.

(21) Péoux, G.; Monnerville, M.; Duhoo, T.; Pouilly, B. *J. Chem. Phys.* **1997**, *107*, 70.

(22) Pouilly, B.; Monnerville, M. *Chem. Phys.* **1998**, *238*, 437.

(23) Baumfalk, R.; Buck, U.; Frischkorn, C.; Nahler, N. H.; Hüwel, L. *J. Chem. Phys.* **1999**, *111*, 2595.

(24) Regan, P. M.; Langford, S. R.; Orr-Ewing, A. J.; Ashfold, M. N. R. *J. Chem. Phys.* **1999**, *110*, 281.

(25) Rakitzis, T. P.; Samartzis, P. C.; Toomes, R. L.; Tsigaridas, L.; Coriou, M.; Chestakov, D.; Eppink, A. T. J. B.; Parker, D. H.; Kitsopoulos, T. N. *Chem. Phys. Lett.* **2002**, *364*, 115.

(26) Rakitzis, T. P.; Samartzis, P. C.; Toomes, R. L.; Kitsopoulos, T. N. *J. Chem. Phys.* **2004**, *121*, 7222.

(27) Smolin, A. G.; Vasyutinskii, O. S.; Balint-Kurti, G. G.; Brown, A. *J. Phys. Chem. A* **2006**, *110*, 5371.

(28) Fárník, M.; Buck, U. *Phys. Scr.* **2007**, *76*, C73.

(29) Levy, I.; Shapiro, M. *J. Chem. Phys.* **1988**, *89*, 2900.

(30) Kalyanaraman, C.; Sathyamurthy, N. *Chem. Phys. Lett.* **1993**, *209* (1, 2), 52.

(31) Gross, P.; Gupta, A. K.; Bairagi, D. B.; Mishra, M. K. *J. Chem. Phys.* **1996**, *104*, 7045.

(32) Gendron, D. J.; Hepburn, J. W. *J. Chem. Phys.* **1998**, *109*, 7205.

(33) Langford, S. R.; Regan, P. M.; Orr-Ewing, A. J.; Ashfold, M. N. R. *Chem. Phys.* **1998**, *231*, 245.

(34) Alekseyev, A. B.; Liebermann, H.-P.; Kokh, D. B.; Buenker, R. J. *J. Chem. Phys.* **2000**, *113*, 6174.

(35) Balakrishnan, N.; Alekseyev, A. B.; Buenker, R. J. *Chem. Phys. Lett.* **2001**, *341*, 594.

(36) Fujisaki, H.; Teranishi, Y.; Nakamura, H. *J. Theor. Comput. Chem.* **2002**, *1* (2), 245.

(37) Camden, J. P.; Bechtel, H. A.; Brown, D. J. A.; Pomerantz, A. E.; Zare, R. N.; Le Roy, R. J. *J. Phys. Chem. A* **2004**, *108*, 7806.

(38) Brown, A. *J. Chem. Phys.* **2005**, *122*, 084301.

(39) Jodoin, D. N.; Brown, A. *J. Chem. Phys.* **2005**, *123*, 054301.

(40) Brown, A. *Int. J. Quantum Chem.* **2007**, *107*, 2665.

(41) Bates, J. R.; Halford, J. O.; Anderson, L. C. *J. Chem. Phys.* **1935**, *3*, 531.

(42) Donovan, R. J.; Husain, D. *Trans. Faraday Soc.* **1966**, *62*, 1050.

(43) Huebert, B. J.; Martin, R. M. *J. Phys. Chem.* **1968**, *72*, 3046.

(44) Compton, L. E.; Martin, R. M. *J. Phys. Chem.* **1969**, *73*, 3474.

(45) Ogilvie, J. F. *Trans. Faraday Soc.* **1971**, *67*, 2205.

(46) LeRoy, R. J.; Kraemer, G. T.; Manzhos, S. *J. Chem. Phys.* **2002**, *117*, 9353.

(47) Mulliken, R. S. *Phys. Rev.* **1937**, *51*, 310.

(48) Mulliken, R. S. *J. Chem. Phys.* **1940**, *8*, 382.

(49) Werner, H.-J.; Knowles, P. J.; Lindh, R.; Manby, F. R.; Schültz, M.; Celani, P.; Korona, T.; Manby, F. R.; Rauhut, G.; Amos, R. D.; Bernhardsson, A.; Berning, A.; Cooper, D. L.; Deegan, M. J. O.; Dobbyn, A. J.; Eckert, F.; Hampel, C.; Hetzer, G.; Lloyd, A. W.; McNicholas, S. J.; Meyer, W.; Mura, M. E.; Nicklass, A.; Palmieri, P.; Pitzer, R.; Schumman, U.; Stoll, H.; Stone, A. J.; Tarroni, R.; Thorsteinsson, T. *MOLPRO: A Package of Ab Initio Programs*, version 2002.6; 2004. http://www.mol-pro.net.

(50) Dunning, T. H., Jr *J. Chem. Phys.* **1989**, *90*, 1007.

(51) Peterson, K. A.; Figgen, D.; Goll, E.; Stoll, H.; Dolg, M. *J. Chem. Phys.* **2003**, *119*, 11113.

(52) Basis sets were obtained from the Extensible Computational Chemistry Environment Basis Set Database, version 02/02/06, as developed and distributed by the Molecular Science Computing Facility, Environmental and Molecular Sciences Laboratory, which is part of the Pacific Northwest Laboratory, P. O. Box 999, Richland, WA 99352, and funded by the U.S. Department of Energy. The Pacific Northwest Laboratory is a multiprogram laboratory operated by Battelle Memorial Institute for the U.S. Department of Energy under Contract No. DE-AC06-76RLO 1830.

(53) Werner, H.-J.; Knowles, P. J. *J. Chem. Phys.* **1985**, *82*, 5053.

(54) Knowles, P. J.; Werner, H.-J. *Chem. Phys. Lett.* **1985**, *115*, 259.

(55) Werner, H.-J.; Knowles, P. J. *J. Chem. Phys.* **1988**, *89*, 5803.

(56) Knowles, P. J.; Werner, H.-J. *Chem. Phys. Lett.* **1988**, *145*, 514.

(57) Werner, H.-J. In *Domain-Based Parallelism and Problem Decomposition Methods in Computational Science and Engineering*; Keyes, D. E., Saad, Y., Truhlar, D. G., Eds.; SIAM: Philadelphia, 1995; pp 239−261.

(58) Blomberg, M. R. A.; Siegbahn, P. E. M. *J. Chem. Phys.* **1992**, *96*, 1218.

(59) Simons, J. *J. Phys. Chem.* **1989**, *93*, 626.

(60) Langhoff, S. R.; Davidson, E. R. *Int. J. Quantum Chem.* **1974**, *8*, 61.

(61) Lichten, W. *Phys. Rev.* **1963**, *131*, 229.

(62) Smith, F. T. *Phys. Rev.* **1969**, *179*, 111.

(63) Macias, A.; Riera, A. *J. Phys. B* **1978**, *11*, L489.

(64) Baer, M. *Mol. Phys.* **1980**, *40*, 1011.

(65) Garrett, B.; Truhlar, D. G. *Theor. Chem.: Adv. Perspect.* **1981**, *6A*, 215.

(66) Delos, J. B. *Rev. Mod. Phys.* **1981**, *53*, 287.

(67) Werner, H.-J.; Meyer, W. *J. Chem. Phys.* **1981**, *74*, 5802.

(68) Cimiraglia, R.; Malrieu, J.-P.; Persico, M.; Spiegelman, F. *J. Phys. B* **1985**, *18*, 3073.

(69) Sidis, V. *Adv. Chem. Phys.* **1992**, *82*, 73.

(70) Pacher, T.; Cederbaum, L. S.; Köppel, H. *Adv. Chem. Phys.* **1993**, *84*, 293.

(71) Yarkony, D. R. *J. Chem. Phys.* **2000**, *12*, 2111.

(72) Zou, P.; McGivern, W. S.; North, S. W. *Phys. Chem. Chem. Phys.* **2000**, *2*, 3785.

(73) Nakamura, H.; Truhlar, D. G. *J. Chem. Phys.* **2001**, *115*, 10353.

(74) Jasper, A. W.; Kendrick, B. K.; Mead, C. A.; Truhlar, D. G. *Adv. Ser. Phys. Chem.* **2004**, *14*, 329.

(75) Köppel, H. *Adv. Ser. Phys. Chem.* **2004**, *15*, 175.

(76) Valero, R.; Truhlar, D. G. *J. Phys. Chem. A* **2007**, *111*, 8536.

(77) Mead, C. A.; Truhlar, D. G. *J. Chem. Phys.* **1982**, *77*, 6090.

(78) Moore, C. E. *Atomic Energy Levels*; Circular 467; National Bureau of Standards: Washington, DC, 1949; Vol. 1−3.

(79) Hack, M. D.; Jasper, A. W.; Volobuev, Y. L.; Schwenke, D. W.; Truhlar, D. G. *J. Phys. Chem. A* **1999**, *103*, 6309.

(80) Bonhommeau, D.; Viel, A.; Halberstadt, N. *J. Chem. Phys.* **2005**, *123*, 054316.

(81) Huber, K. P.; Herzberg, G. *Molecular Spectra and Molecular Structure IV. Constant of Diatomic Molecules*; Van Nostrand: Princeton, NJ, 1979.

(82) Marquardt, D. W. *J. Soc. Appl. Math.* **1963**, *2*, 431.

(83) http://www.gnuplot.info.

(84) Sakurai, J. J. *Modern Quantum Mechanics*; Addison-Wesley: Reading, 1985; pp 335−339.

(85) Schinke, R. *Photodissociation Dynamics*; Cambridge University Press: Cambridge, U.K., 1993.

(86) Wigner, E. *Phys. Rev.* **1932**, *40*, 749.

(87) Press, W. H.; Teukolsky, S. A.; Vetterling, W. T.; Flannery, B. P. *Numerical Recipes in FORTRAN*, 2nd ed.; Cambridge University Press: Cambridge, U.K., 1994; p 279.

(88) Jasper, A. W.; Zhu, C.; Nangia, S.; Truhlar, D. G. *Faraday Discuss.* **2004**, *127*, 1.

(89) Jasper, A. W.; Nangia, S.; Zhu, C.; Truhlar, D. G. *Acc. Chem. Res.* **2006**, *39*, 101.

(90) Tully, J. C. *J. Chem. Phys.* **1990**, *93*, 1061.

(91) (a) Jasper, A. W.; Stechmann, S. N.; Truhlar, D. G. *J. Chem. Phys.* **2002**, *116*, 5424. (b) Jasper, A. W.; Stechmann, S. N. *J. Chem. Phys.* **2002**, *117*, 10427E

(92) Jasper, A. W.; Truhlar, D. G. *Chem. Phys. Lett.* **2003**, *369*, 60.

(93) Jasper, A. W.; Truhlar, D. G. *J. Chem. Phys.* **2007**, *127*, 194306.

(94) Zhu, C.; Nangia, S.; Jasper, A. W.; Truhlar, D. G. *J. Chem. Phys.* **2004**, *121*, 7658.

(95) Zhu, C.; Jasper, A. W.; Truhlar, D. G. *J. Chem. Phys.* **2004**, *120*, 5543.

Photodissociation of HBr

J. Phys. Chem. A, Vol. 112, No. 25, 2008 **5769**

(96) Truhlar, D. G.; Muckerman, J. T. In *Atom-Molecule Collision Theory: A Guide for the Experimentalist*; Bernstein, R. B., Ed.; Plenum Press: New York, 1979; pp 505−566.

(97) Chałasiński, G.; Szczęśniak, M. M. *Chem. Rev.* **2000**, *100*, 4227.

(98) Alekseyev, A. B.; Liebermann, H.-P.; Buenker, R. J.; Yurchenko, S. N. *J. Chem. Phys.* **2007**, *126*, 234103.

(99) Berning, A.; Schweizwer, M.; Werner, H.-J.; Knowles, P. J.; Palmieri, P. *Mol. Phys.* **2000**, *98*, 1823.

(100) (a) Dunning, T. H., Jr *J. Chem. Phys.* **1989**, *90*, 1007. (b) Kendall, R. A.; Dunning, T. H., Jr.; Harrison, R. J. *J. Chem. Phys.* **1992**, *96*, 6796.

(101) Wilson, A. K.; Woon, D. E.; Peterson, K. A.; Dunning, T. H., Jr *J. Chem. Phys.* **1999**, *110*, 7667.

(102) Schmidt, M. W.; Baldridge, K. K.; Boatz, J. A.; Elbert, S. T.; Gordon, M. S.; Jensen, J. H.; Koseki, S.; Matsunaga, N.; Nguyen, K. A.; Su, S. J.; Windus, T. L.; Dupuis, M.; Montgomery, J. A. *J. Comput. Chem.* **1993**, *14*, 1347.

(103) Kłos, J.; Szczēśniak, M. M.; Chałasiński, G. *Int. Rev. Phys. Chem.* **2004**, *23*, 541.

(104) Alexander, M. H.; Manolopoulos, D. E.; Werner, H.-J. *J. Chem. Phys.* **2000**, *113*, 11084.

(105) Grinev, T. A.; Tscherbul, T. V.; Buchachenko, A. A.; Cavalli, S.; Aquilanti, V. *J. Phys. Chem. A* **2006**, *110*, 5458.